Angular and Radial Directivity Control for Spherical Loudspeaker Arrays

Diploma Thesis
by
Hannes Pomberger

Institute of Electronic Music and Acoustics
University of Music and Dramatic Arts, Graz - Austria

Supervisors: Univ.Ass. DI Dr.techn. Alois Sontacchi
DI Franz Zotter

Assessor: O.Univ.Prof. Mag.art. DI Dr.techn. Robert Höldrich

April 2008

ABSTRACT

Spherical loudspeaker arrays, as concerned within this work, are a finite set of transducers distributed on the surface of a sphere or platonic solid. The purpose of these arrays is to synthesize artificial acoustic radiation or to reproduce natural sound sources. This relatively recent research topic is applicable in many fields, such as musical performances or acoustic measurements. The present thesis develops and discusses a control system for directivity pattern synthesis using an icosahedral loudspeaker array. In order to obtain sensible control parameters a surrounding spherical microphone array is used to measure the individual directivities of the array transducers. Basically, weighted combinations can be computed to create a variable directivity directly at the measurement radius. It is, however, advantageous to decompose these directivities into orthogonal spherical harmonic components. At this radius the spherical harmonics provide directivity synthesis with well defined angular resolution and simple relations for rotation of synthesis patterns. Arbitrarily, synthesis patterns will appear blurred at other radii due to sound propagation. Inherently, the spherical harmonics are affected by well-defined gain and phase changes but retain their individual shape. Efficient time-domain radial steering filters are introduced to focus the synthesis pattern to variable radii. The limitations of the over-all control systems are being investigated.

ABSTRACT

Die in der vorliegenden Arbeit beschriebenen sphärischen Lautsprecher-Arrays bestehen aus einer endlichen Anzahl von elektro-akustischen Wandlern, welche auf der Oberfläche einer Kugel oder eines platonischen Körpers verteilt sind. Mit diesen Arrays sollen künstliche akustische Abstrahlungen synthetisiert, sowie jene von natürlichen Schallquellen nachgebildet werden. Das relativ junge Forschungsthema kann in vielen Bereichen Anwendung finden, wie z.B. bei musikalischen Aufführungen oder in der akustischen Messtechnik. Diese Arbeit entwickelt eine Steuerung zur Synthese von Abstrahlcharakteritiken mit einem ikosaederförmigen Array. Um geeignete Steuerparameter zu erhalten, wird mit einem umgebenden, kugelförmigen Mikrofon-Array die individuelle Abstrahlung der einzelnen Lautsprecher gemessen. Bereits durch die Berechnung einer gewichteten Kombination der Wandlersignale ergibt sich eine variable Richtcharakteristik am Radius der Messanordnung. Es ist jedoch von Vorteil, diese Abstrahlungsmuster in orthogonale Komponenten (Kugelflächenfunktionen) zu zerlegen. Dadurch werden eine gleichmäßige Winkelauflösung und einfache Rotationsvorschriften für die synthetisierten Richtmuster erreicht. An anderen Radien werden jedoch synthetisierte Richtmuster im Allgemeinen unscharf, da sie sich aufgrund der Schallausbreitung verändern. Die Kugleflächenfunktionen behalten ihre ursprüngliche Form und zeigen ausbreitungsbedingt nur Amplituden- und Phasenänderungen. Durch die Einführung effizienter zeitdiskreter radialer Steuerungsfilter wird eine Fokussierung der synthetisierten Richtmuster auf variable Radien bewirkt. Weiters werden die Grenzen eines gesamten Steuersystems untersucht.

Contents

Chapter I

INTRODUCTION

The perceptual impact of live played instruments results not only from the direct sound but also from the interaction with the room. Therefore the acoustic signature of sound sources consists of a specific frequency spectrum as well as a frequency dependent directivity pattern, representing the distribution of the radiated sound over the solid angle. However, an instrument reproduced over a single loudspeaker will be perceived differently than played live, even if its spectral components are synthesized well, since the loudspeaker imposes its specific directivity to the radiated sound and thus provides a different stimulus for the room.

Consequently, a need for electro-acoustic devices with adjustable directivity arises for proper synthesis of acoustic sources. Such devices especially suited for acoustic radiation synthesis consist of a several individually controllable loudspeakers arranged on a solid sphere or convex polyhedron and are commonly referred to as spherical loudspeaker arrays. In general, a uniform distribution of the transducers over the whole solid angle is desirable and most prototypes of spherical loudspeaker arrays achieve this by having the transducer mounted on the faces of platonic solids such as cubes, dodecahedrons or icosahedrons.

Controllable directivity patterns also allow reproduction of time varying directivities caused by the movements of musicians when playing an instrument. Beyond a more authentic reproduction of natural sound sources, these devices will find application in room acoustic measurements. At present usually omni directional sound sources are used, but spherical loudspeaker arrays will make measurements with different excitation directivities possible. This leads to a more detailed exploration of room acoustic properties, e.g. how the room reacts on specific sources or for tracing reflections by selective excitation.

Recently, several publications have been released concerning directivity pattern synthesis with spherical loudspeaker arrays. Warusfel presented in [WDC97] a basic method to approximate radiation patterns of musical instruments by finding and appropriate linear combination of the individual loudspeaker patterns via optimization. Kassakian and Wessel pointed out the error bounds of pattern approximation for several array geometries in [KW04]. Unsurprisingly, it has shown that with an increasing number of drivers more complex target patterns can be reproduced. Zotter described the behavior of spherical loudspeaker arrays analytically in [ZH07] by modeling each loudspeaker as vibrating sphere cap. This model has also been used to describe the synthesis errors of some spherical layouts in terms of frequency and distance. The extended model in [ZSH07] takes the acoustic coupling between individual loudspeakers sharing a common enclosure into account. In an attempt to verify the analytic model, laser Doppler vibromentry measurements from a real icosahedral array have been compared to computer simulations. Pollow presented in his master thesis [Pol07] a method to reproduce instrument specific directivity patterns using a magnitude optimization approach and a dodecahedral array for the purpose of room acoustic measurements.

This work revises and develops a control theory for spherical loudspeaker arrays based on measurements, and arrives at compact expressions that can be efficiently implemented. In a first step, it will be shown how a suitable system for angular directivity control can be determined from acoustic measurements of the loudspeaker array with a surrounding microphone array. The radius of the synthesis sphere is thereby predetermined by the radius of the microphone array. Due to sound propagation, synthesized patterns will appear blurred at other radii. To overcome the restriction to a fixed synthesis radius, a radial directivity control will be introduced allowing the displacement of synthesized patterns to desired radii. This is achieved by a set of efficient time-domain filters compensating for the radial wave propagation.

1.1 Preview of Thesis

Chapter 2

By preliminary acoustic measurements with a surrounding microphone array the directivities of the individual array transducers are determined. The theoretical background for expanding functions on the sphere into the orthonormal base of spherical harmonics is revisited briefly. Moreover, the sampling problem on the sphere is considered and different layouts for spherical sampling grids are discussed. Finally, an appropriate directivity control is developed based on the measured data, and simulation results alongside with a detailed analysis of synthesis errors are given.

Chapter 3

Considering the radial solution of the wave equation, analytic expressions representing the sound propagation are derived. To compensate for the propagation adequate radial steering filters are introduced. Based on the analytic expressions efficient discrete-time implementations of these filters are achieved via bilinear transform and newly impulse invariance variations. Considering the approximation error relative to the continuous-time functions, the different filter implementations are evaluated on concrete examples.

Chapter 4

This chapter gives a brief summary of what has been achieved during this work.

Chapter II

ANGULAR DIRECTIVITY CONTROL

2.1 Introduction

In this chapter a control system for directivity pattern synthesis with a spherical (in particular icosahedral) loudspeaker array is developed considering a fixed radial synthesis distance.

In a first step the directivity patterns of each individual transducer will be measured by a spherical microphone array surrounding the icosahedral array. The surface of this microphone array, concentric to the loudspeaker array, also specifies surface of the synthesis process. Basically, the directivity of the entire loudspeaker array is composed as a linear combination of the individual transducer patterns. Hence, a desired directivity for the entire array can be approximated by weighting the individual transducers in a sensible way. For the best approximation of desired radiation pattern this frequency dependent weights could be determined by an optimization algorithm.

Alternatively, the transducer patterns, and the desired array directivity as well, can be decomposed into a set orthonormal base functions, most suitably the spherical harmonics. In this spirit, the complete the synthesis problem is transformed into the spherical harmonics domain. Due to the orthogonality of the base functions this representation shows several advantages. Directivity synthesis in terms of spherical harmonics provides a well defined angular resolution and simple relations for pattern rotation. As we will see in chapter 3, it also allows for a radial directivity control.

The IEM Icosahedral Loudspeaker Array: Considering its simplicity in construction and given a limit in the amount of speakers, the regular icosahedron was chosen as basic shape for the spherical array. Due to its symmetry, mounting the speakers at the center of the twenty faces provides a uniform spatial distribution of the array elements. The loudspeaker array was primarily designed for reproduction of Javanese gong instruments and has a lower frequency bound of $f_0 = 43$Hz. The size of the icosahedral body can be described by a circumscribed sphere of the radius $r_u = 33$cm, touching the icosahedron at all vertices. The corresponding driver spacing is 19cm. A rough rule-of-thumb estimate of the upper cut-off frequency for spatial aliasing yields $f_u = 1$kHz. For more information about design considerations and construction issues of IEM icosahedral array the reader is referred to [ZS07].

2.2 Measurements

Setup: For the measurements a configuration of 648 microphones distributed on a sphere surface with a radius of $0.7m$, centered around the icosahedral loudspeaker-array, was chosen. Figure 1 depicts the grid layout consisting of 18 latitude circles located in 10° steps symmetric to the equator and 36 equidistant meridians also spaced in 10° steps. To reduce the hardware effort, each meridian of the grid was measured sequentially by a fixed semicircular array while rotating the icosahedron on a turn table, see Figure 2. Details on the spatial sampling configuration will be given in a latter section.

The impulse responses of the loudspeaker-to-microphone transmission paths where measured by the exponentially-swept sine technique presented by Farina in [Far00]. By default of an anechoic chamber the measurements were performed in an acoustically damped room. To allow for the flight time of the impulse responses through the interior of the icosahedral array a complete removal of the acoustic echoes of the measurement chamber by temporal windowing is not possible. Thus the free-field responses of the transducers are probably corrupted by some of the first reflections.

MIMO-Description: With the measured impulse responses $g_{ij}(t)$ of the transmission paths from loudspeaker i to microphone j, the system can be modeled as a linear $K \times L$ multiple-input-multiple-output (MIMO) system, where $K = 648$ is the number of

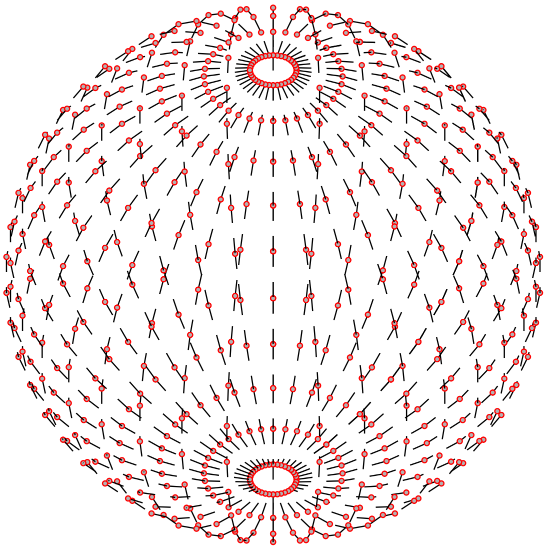

Figure 1: Sampling Layout

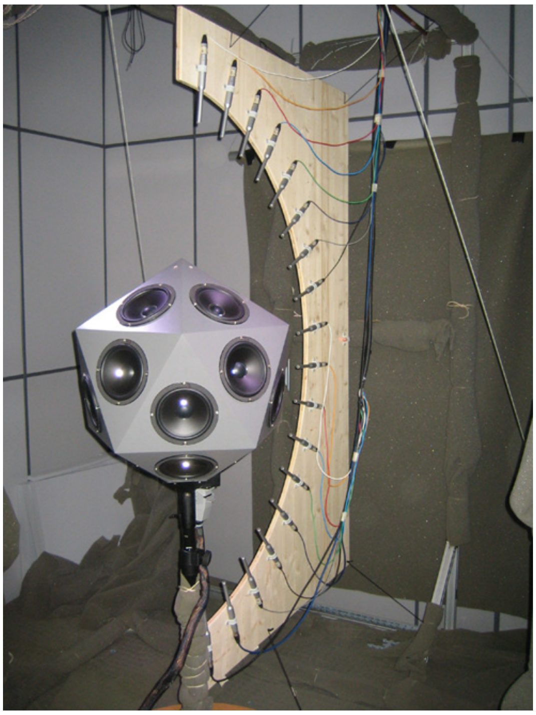

Figure 2: Icosahedron and Semicircular Microphone Array

microphones of the spherical array and $L = 20$ is the number of loudspeakers of the icosahedral array. The sketch in Figure 3 depicts the MIMO-system with time domain symbols.

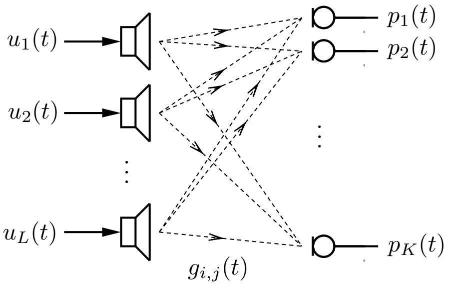

Figure 3: MIMO-System

The sound pressure at each microphone position results from superposition of the loudspeaker excitation signals convolved with the corresponding transmission paths. In the frequency domain this can be expressed straightforward as matrix multiplication:

$$\boldsymbol{p}(\omega) = \boldsymbol{G}(\omega) \cdot \boldsymbol{u}(\omega) \tag{2.1}$$

where $\boldsymbol{G}(\omega)$ is a 648×20-matrix, containing the Fourier transform of the measured impulse responses. One row of $\boldsymbol{G}(\omega)$ is depicted in Figure 4 and represents the measured

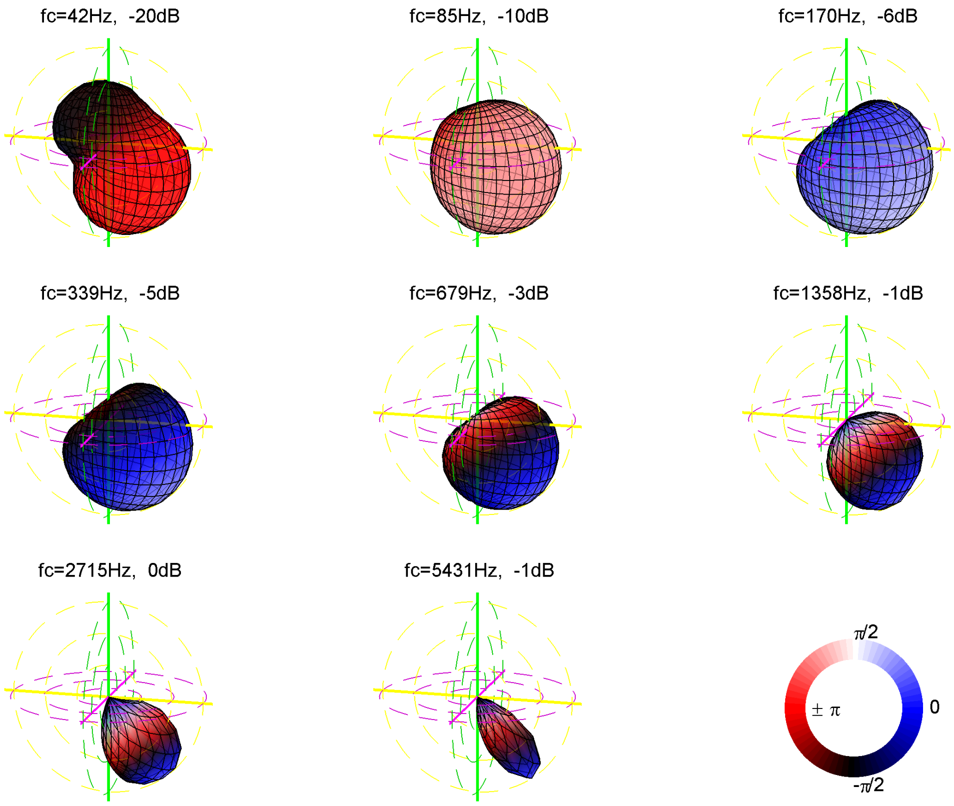

Figure 4: Normalized directivity pattern of one individual loudspeaker in octave bands (30db dynamic range, the dashed circles indicate 10dB steps, for each band the center frequency and the normalization factor are specified)

directivity of one individual loudspeaker. Note that in the following the indication of the frequency dependence will be omitted for better readability, but the relations will hold only in the frequency domain.

Microphone Equalization: For the semicircular array, 18 low-cost measurement microphones were used. To compensate for their possible insufficiently flat magnitude responses, a reference measure comparing each low-cost microphone to a high-quality measurement microphone was taken, see Figure 5. Following the method proposed by Pei and Lin in [PL06], 18 minimum-phase FIR filters were designed based on the magnitude relation between each low-cost microphone and the high-quality microphone. The application of these equalization filters to the measure equalizes the frequency-response of the measurement chain.

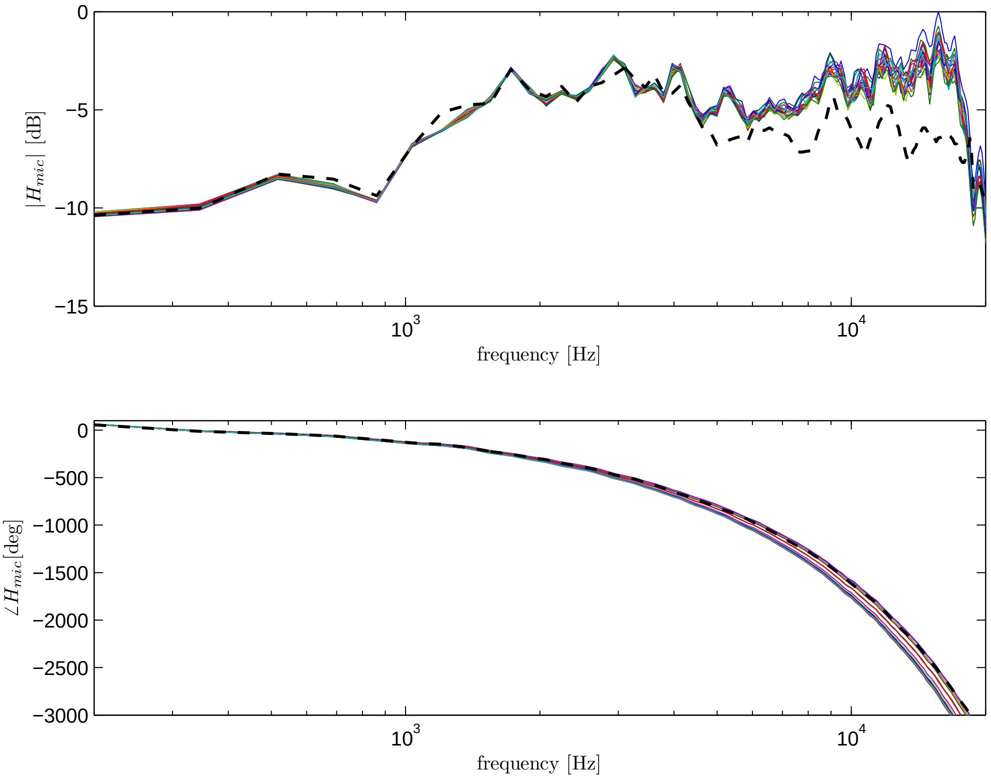

Figure 5: Frequency responses of the 18 low-cost measurement microphones (colored lines) and the high-quality measurement microphone (dashed black line)

2.3 Synoptic View

The MIMO-system measured in the previous section is represented by the centerpiece of the block diagram depicted in Figure 6. Based on the spatial sampling due to the measurement grid, a discrete spherical harmonics transform needs to be developed and applied to the measurement data. This step, represented by the box on the right side, yields a transformed MIMO-system with the loudspeaker excitation signals $[u_1, u_2, \cdots, u_L]$ at its input, and sound pressure values decomposed into spherical harmonics[1] at the measurement sphere $[\psi_0^0, \psi_1^{-1}, \cdots \psi_{N_a}^{N_a}]$ at the output. Finally, a proper inversion of the transformed MIMO-system is required to control the array transducers, represented by the box on the left side in Figure 6. This control system converts a desired directivity pattern specified by its spherical harmonics components $[\gamma_0^0, \gamma_1^{-1}, \cdots \gamma_{N_c}^{N_c}]$ to filter weights for the transducer signals, such that $[\psi_0^0, \psi_1^{-1}, \cdots \psi_{N_a}^{N_a}]$ yields the best approximation.

---

[1] The weird indexing of the spherical harmonics will be clarified in the subsequent section.

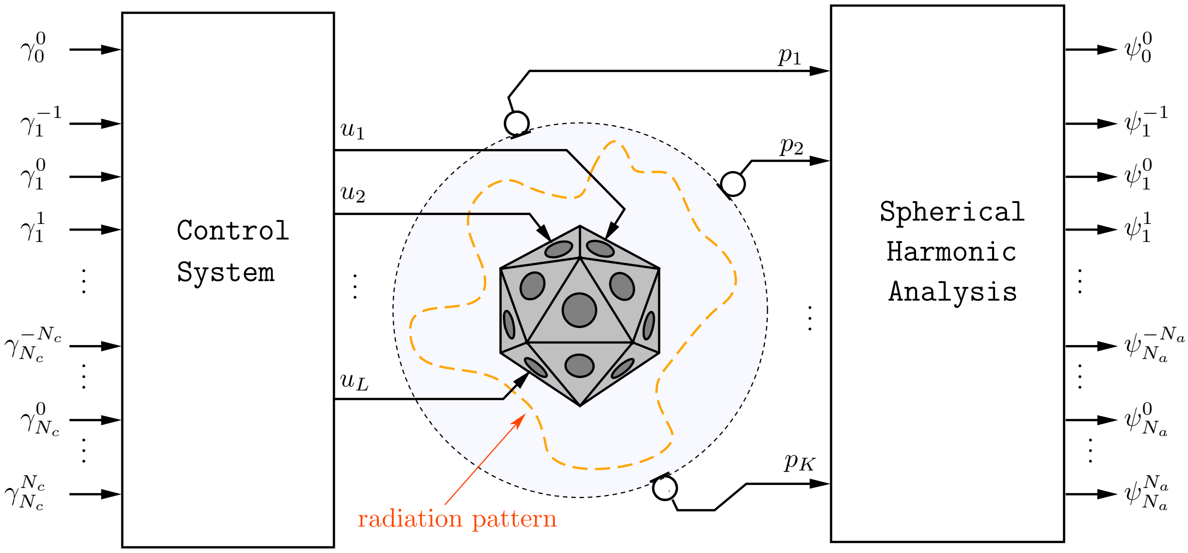

Figure 6: Block Diagramm

2.4 *Fourier Expansion on the Sphere*

Spherical Harmonics Expansion: Any square integrable function $x(\boldsymbol{\theta})$ on the unit sphere can be expressed as a linear combination of special functions $Y_n^m(\boldsymbol{\theta})$, known as spherical harmonics:

$$x(\boldsymbol{\theta}) = \sum_{n=0}^{\infty} \sum_{m=-n}^{n} \chi_{nm} Y_n^m(\boldsymbol{\theta}) \tag{2.2}$$

where χ_{nm} are the expansion coefficients[1] and $\boldsymbol{\theta} \equiv (\varphi, \theta)$ denotes a pair of angular coordinates. The spherical harmonics are a complete set of orthonormal functions in the Hilbert space $L^2(S^2)$, such that

$$\int\limits_{S^2} Y_n^m(\boldsymbol{\theta}) Y_{n'}^{m'*}(\boldsymbol{\theta}) d\boldsymbol{\theta} = \delta_{nn'}\delta_{mm'} \tag{2.3}$$

where δ_{ij} denotes Kronecker's delta. Thus the Fourier coefficients are obtained from the inner product:

$$\chi_{nm} = \int_{S^2} x(\boldsymbol{\theta}) Y_n^{m*}(\boldsymbol{\theta}) d\boldsymbol{\theta} \tag{2.4}$$

with $\int_{S^2} d\boldsymbol{\theta} \equiv \int\limits_0^{2\pi} \int\limits_0^{\pi} \sin(\theta) d\theta d\varphi$ and * denotes complex conjugation. The integer values n and m will be referred to as order and degree of the spherical harmonics and a function

---

[1] During this work the following convention is used: The coefficients of the spherical harmonic expansion of a function are denoted by corresponding Greek letters.

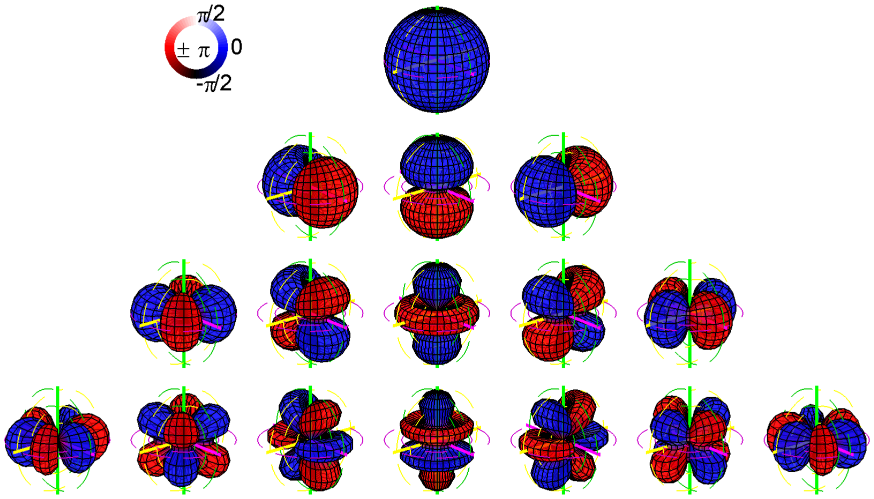

Figure 7: Spherical harmonic base functions up to order $n = 3$

$x(\boldsymbol{\theta})$ for which all Fourier coefficients of order $n > N$ are equal to zero will be referred to as a band-limited function on the sphere with maximum order N.

As for the ordinary Fourier transform, either real valued or complex base functions can be defined. Complex base functions are necessary to transform analytic signals. During this work we only consider real valued signals, due the physical meaning of sound pressure and particle velocity. Hence we are free to choose the real valued base functions which are defined as:

$$Y_n^m(\varphi,\theta) \equiv \begin{cases} \sqrt{\frac{(2n+1)}{4\pi}\frac{(n-m)!}{(n+m)!}}P_n^m(\cos\theta)\sqrt{2-\delta_{m0}}\cos(m\varphi) & \text{if } m \geq 0 \\ \sqrt{\frac{(2n+1)}{4\pi}\frac{(n-m)!}{(n+m)!}}P_n^m(\cos\theta)\sqrt{2}\sin(m\varphi) & \text{if } m < 0 \end{cases} \tag{2.5}$$

where $P_n^m(x)$ are the associated Legendre functions. Knowing that $P_0^0(x) = 1$ and $P_1^0(x) = x$ the associated Legendre functions can be developed using the following recurrence relations:

$$(2n+1)xP_n^m(x) = (n-m+1)P_{n+1}^m(x) + (n+m)P_{n-1}^m(x) \tag{2.6}$$

$$P_n^{m+2}(x) = -2(m+1)\frac{x}{\sqrt{1-x^2}}P_n^{m+1}(x) - (n-m)(n+m+1)P_n^m(x) \tag{2.7}$$

$$P_{n-1}^m - P_{n+1}^m(x) = (2n+1)\sqrt{1-x^2}P_n^{m-1}(x) \tag{2.8}$$

Figure 7 shows the first 16 spherical harmonics up to order $n = 3$ defined like in (2.5). Note that due to the choice of real spherical harmonic base functions, the complex-conjugation in Eq.(2.4) is irrelevant and hence will be omitted in further developments.

Spherical Wave Spectrum: The spherical wave spectrum, like defined in Williams [Wil99], is the application of the spherical Fourier expansion to an acoustic field quantity on a sphere surface of radius r_i:

$$\chi_{nm}(r_i) \equiv \int_{S^2} x(r_i, \varphi, \theta) Y_n^m(\boldsymbol{\theta}) d\boldsymbol{\theta} \tag{2.9}$$

where $\chi_{nm}(r_i)$ represents the the spherical wave components at r_i. Due to our nomenclature, $\psi_{nm}(r_i)$ will denote the spherical pressure spectrum and $\Upsilon_{nm}(r_i)$ the spherical particle velocity spectrum.

2.5 Sampling the Sphere - General Remarks

In practice continuous functions are determined by a finite number of sample values obtained by a set of transducers located at $\boldsymbol{\theta}_k$. A useful notation, according to Zotter in [ZH07], is introduced to provide compact matrix notations. We define a band-limited $(N+1)^2$-element spherical harmonics coefficient vector $\boldsymbol{c}_{SH,N}^{(k)}$ and a $(N+1)^2 \times K$ matrix $\boldsymbol{C}_{SH,N}$ as:

$$\boldsymbol{c}_{SH,N}^{(k)} = \mathrm{vec}_{SH,N}\left\{Y_n^m(\boldsymbol{\theta}_k)\right\} \equiv \begin{bmatrix} Y_0^0(\boldsymbol{\theta}_k) \\ Y_1^{-1}(\boldsymbol{\theta}_k) \\ \vdots \\ \left.\begin{matrix} Y_n^{-n}(\boldsymbol{\theta}_k) \\ \vdots \\ Y_n^n(\boldsymbol{\theta}_k) \end{matrix}\right\} 2n+1 \\ \vdots \\ Y_N^N(\boldsymbol{\theta}_k) \end{bmatrix}, \quad \boldsymbol{C}_{SH,N} \equiv \begin{bmatrix} \boldsymbol{c}_{SH,N}^{T(1)} \\ \boldsymbol{c}_{SH,N}^{T(2)} \\ \vdots \\ \boldsymbol{c}_{SH,N}^{T(K)} \end{bmatrix} \tag{2.10}$$

where K is the number of sample values and N is the maximum spherical harmonics order. Infinitively long vectors, viz. $N \to \infty$, will be indicated by skipping the subscript for the band-limitation. Defining a K-element sample vector $\boldsymbol{x} = [x(\boldsymbol{\theta}_1), x(\boldsymbol{\theta}_2), \ldots, x(\boldsymbol{\theta}_K)]^T$

and a vector $\chi_{SH} = \mathrm{vec}_{SH}\{\chi_{mn}\}$ containing the expansion coefficients, Eq.(2.2) can be rewritten as matrix equation:

$$\boldsymbol{x} = \boldsymbol{C}_{SH}\,\boldsymbol{\chi}_{SH} \tag{2.11}$$

If non-band-limited functions are sampled with a finite number of samples, the system in Eq.(2.11) is highly under-determined, having an infinite number of solutions. That causes different continuous functions to become indistinguishable due to identical sampling values. In analogy to discrete-time signal processing, this effect is referred to as spatial aliasing.

Assuming an band-limited function on the sphere with maximum order N, the right side of Eq.(2.11) can be truncated to $\boldsymbol{C}_{SH,N}$ and $\boldsymbol{\chi}_{SH,N}$:

$$\boldsymbol{x} = \boldsymbol{C}_{SH,N}\,\boldsymbol{\chi}_{SH,N} \tag{2.12}$$

Depending on the number of sampling points, there exist three cases for Eq.(2.12):

- If $K < (N+1)^2$, the system is under-determined, having an infinite number of exact solutions.
- If $K = (N+1)^2$, the system can be solved exactly, if $\boldsymbol{C}_{SH,N}^{-1}$ exists.
- If $K > (N+1)^2$, the system is over-determined, having no exact solution.

In the over-determined case, an approximate solution for Eq.(2.12) can be determined in a least squares sense by minimizing the squared error norm:

$$\min_{\chi_{SH,N}} \left\|\boldsymbol{x} - \boldsymbol{C}_{SH,N}\hat{\boldsymbol{\chi}}_{SH,N}\right\|_2^2 \tag{2.13}$$

where $\hat{\chi}_{SH,N}$ is the approximated coefficient vector. The squared error norm can be computed as:

$$\begin{aligned}&(\boldsymbol{x} - \boldsymbol{C}_{SH,N}\hat{\boldsymbol{\chi}}_{SH,N})^T(\boldsymbol{x} - \boldsymbol{C}_{SH,N}\hat{\boldsymbol{\chi}}_{SH,N}) =\\ &\boldsymbol{x}\boldsymbol{x}^T - \hat{\boldsymbol{\chi}}_{SH,N}^T\boldsymbol{C}_{SH,N}^T\boldsymbol{x} - \boldsymbol{x}^T\boldsymbol{C}_{SH,N}\hat{\boldsymbol{\chi}}_{SH,N} + \hat{\boldsymbol{\chi}}_{SH,N}^T\boldsymbol{C}_{SH,N}^T\boldsymbol{C}_{SH,N}\hat{\boldsymbol{\chi}}_{SH,N}\end{aligned} \tag{2.14}$$

Differentiating[1] w.r.t $\hat{\chi}^T_{SH,N}$ and setting the result equal zero minimizes the squared error-norm:

$$-\boldsymbol{C}^T_{SH,N}\boldsymbol{x} + \boldsymbol{C}^T_{SH,N}\boldsymbol{C}_{SH,N}\hat{\chi}_{SH,N} = 0 \tag{2.15}$$

By reordering the estimator for the coefficient vector is obtained:

$$\hat{\chi}_{SH,N} = \left(\boldsymbol{C}^T_{SH,N}\boldsymbol{C}_{SH,N}\right)^{-1}\boldsymbol{C}^T_{SH,N}\boldsymbol{x} \tag{2.16}$$

Thus the best band-limited approximation of $\boldsymbol{x}$ in a least squares sense is given by $\chi_{SH,N}$. It is easy to see, that if $\boldsymbol{x}$ is indeed a band-limited function on the sphere, such that it can be expressed by Eq.(2.12), the solution is even exact:

$$\hat{\chi}_{SH,N} = \underbrace{\left(\boldsymbol{C}^T_{SH,N}\boldsymbol{C}_{SH,N}\right)^{-1}\boldsymbol{C}^T_{SH,N}\boldsymbol{C}_{SH,N}}_{\boldsymbol{I}}\ \chi_{SH,N} \tag{2.17}$$

The matrix product in Eq.(2.16) is left-inverse to $\boldsymbol{C}_{SH,N}$ and it is widely known as the Moore-Penrose pseudo inverse[2]. In this work, the pseudo inverse of a matrix $\boldsymbol{A}$ will be denoted by $\boldsymbol{A}^+$ and thus Eq.(2.16) can be denoted for a function $\boldsymbol{x}$ band-limited on the sphere with maximum order N as:

$$\chi_{SH,N} = \boldsymbol{C}^+_{SH,N}\boldsymbol{x} \tag{2.18}$$

Spatial Sampling Theorem: From the previous considerations, it deduces that for an aliasing free estimation of the Fourier coefficients, the following conditions needs be fulfilled. Basically as many sample values are required as spherical harmonics base functions. Moreover the sample values need to distribute in a sensible way, so that the the problem is well-conditioned. These two conditions are expressed by:

$$K \overset{!}{\geq} (N+1)^2 \tag{2.19}$$

$$\kappa\left(\boldsymbol{C}^T_{SH,N}\boldsymbol{C}_{SH,N}\right) << \infty \tag{2.20}$$

where $\kappa(\boldsymbol{A})$ denotes the condition number of a matrix $\boldsymbol{A}$.

---

[1] The calculation rules for matrix differentiation are given in Hjørungnes [HG06]

[2] In the following we will refer to the Moore-Penrose inverse as simply the pseudo inverse.

Aliasing Error: Assume K properly distributed sampling points, where $K \geq (N+1)^2$, so that the Fourier coefficients of band-limited functions up to a maximum order of N can be determined by Eq.(2.16). If we insert a function $\boldsymbol{x} = \boldsymbol{C}_{SH,\tilde{N}}\ \boldsymbol{\chi}_{SH,\tilde{N}}$ violating the sampling condition, viz. $\tilde{N} > N$, we get:

$$\begin{aligned} \boldsymbol{\chi}_{SH,N} &= \boldsymbol{C}^{+}_{SH,N}\boldsymbol{C}_{SH,\tilde{N}}\ \boldsymbol{\chi}_{SH,\tilde{N}} \\ &= \boldsymbol{C}^{+}_{SH,N}\left[\boldsymbol{C}_{SH,N}, \boldsymbol{C}_{SH,N\to\tilde{N}}\right] \boldsymbol{\chi}_{SH,\tilde{N}} \\ &= \left[\underbrace{\boldsymbol{C}^{+}_{SH,N}\boldsymbol{C}_{SH,N}}_{\boldsymbol{I}}, \underbrace{\boldsymbol{C}^{+}_{SH,N}\boldsymbol{C}_{SH,N\to\tilde{N}}}_{E_{SH,N\to\tilde{N}}}\right] \boldsymbol{\chi}_{SH,\tilde{N}} \end{aligned} \tag{2.21}$$

where $\boldsymbol{C}_{SH,N\to\tilde{N}}$ denotes the $(\tilde{N}+1)^2 - (N+1)^2$ rows left in $\boldsymbol{C}_{SH,\tilde{N}}$ corresponding to the spherical harmonics of order $n > N$. Due to the fact that $\boldsymbol{C}^{+}_{SH,N}$ is left inverse to $\boldsymbol{C}_{SH,N}$, the left side of the matrix product in Eq. (2.21) is the $(N+1)^2 \times (N+1)^2$ identity matrix, indicated by $\boldsymbol{I}$. However the right side, indicated by $E_{SH,\tilde{N}\to N}$, is likely to differ from an all-zero matrix. Thus the non-zero elements in $E_{SH,\tilde{N}\to N}$ project the higher order components of $\boldsymbol{\chi}_{SH,\tilde{N}}$ onto $\boldsymbol{\chi}_{SH,N}$. This represents the spatial aliasing error.

2.6 Sampling Configurations:

Distributing a certain number of samples judiciously on a sphere, such that both conditions stated in Eq.(2.20) are fulfilled, is not a trivial problem. Like already mentioned, there exist a few uniform sampling grids associated with the platonic solids, but these are limited to maximum order of $N = 3$. Furthermore there are design methodologies to find quasi-uniform distribution, like spherical t-design, cf. Hardin [Har96]. On the other hand a classical approach traces back to Gauss (1839) and Neumann (1838), cf. Sneeuw [Sne94]. These layouts, i.e. equiangular sampling and Gaussian-sampling[1], re-establish the orthogonality of the spherical harmonics via quadrature weights, which renders matrix inversion unnecessary. But instead of $(N+1)^2$ samples, these grid layouts require $\approx 4(N+1)^2$ respectively $\approx 2(N+1)^2$ sampling points. Moreover, approaches

---

[1] In [Sne94] they are referred to as First and Second Neumann Method.

exist trying to find proper layouts by iterative optimization, e.g. by Li and Duraiswami in [LD07] where layouts with sufficiently low condition numbers are optimized for.

Due to construction issues, the implementation of the microphone array in section 2.2 required a grid layout, providing a regular structure of sampling points, so that each meridian of the grid can be measured sequentially. In the following, two grid layouts will be discussed fulfilling this requirement.

2.6.1 Equiangular Grid Layout

Equiangular sampling is a very popular grid layout widely treated in literature and quadrature weights are easily determined. Referring to Sneeuw [Sne94] and Driscoll [DH94], a resolution of $J = 2(N+1)$ sampling points in both angular directions (φ, θ) is required for band-limited functions on the sphere up to order N to avoid spatial aliasing. Therefrom deduces that altogether a number of

$$K = 4(N+1)^2 \tag{2.22}$$

samples is required and the angular distances of the grid nodes along the meridians and the equator are:

$$\Delta\varphi = \frac{2\pi}{J} \qquad \Delta\theta = \frac{\pi}{J} \tag{2.23}$$

The grid is assumed to be symmetric to the equator and the angular position vector of the sample nodes are linearly indexed by $k = 0, 1, \cdots, K-1$. The angular position $\boldsymbol{\theta}_k$ of a grid-node k is determined by:

$$\boldsymbol{\theta}_k = \left[\ \Delta\phi \cdot \mathrm{div}\,(k, J)\ ,\ \Delta\theta \cdot \left(\mathrm{mod}\,(k, J) + \frac{1}{2}\right)\right] \tag{2.24}$$

Thereby the node with index $k = 0$ is the point next to the north pole on the prime meridian. With increasing k the rest of the nodes on the prime meridian follow in order of their elevation and subsequently the following meridian are traversed in the same direction.

Neumann's Exact Quadarture Method: The equiangular grid is a non-orthogonal sampling in terms of Legendre polynomials. In contrast, the sine and cosine terms, uniformly sampled in longitude direction, stay orthogonal. Therefore recovering the orthogonality of the Legendre polynomials also re-establishes the the orthogonality of the spherical harmonics. Exact orthogonality can be attained for the discretized Legendre polynomials by devising certain quadrature weights w_i. For a grid symmetric to the equator the quadrature weights are symmetric as well. Accordingly, we only consider the $N+1$ latitude circles of one hemisphere to determine these weights, which have to fulfill the following condition, given in cf. [Sne94]:

$$\sum_{i=1}^{N+1} \frac{1}{2}(2-\delta_{N+1,i}) w_i \cos(2n\theta_i) = \frac{-1}{4n^2-1}, \qquad n = 0, 1, \cdots, N \tag{2.25}$$

This leads to the following matrix equation to determine the quadrature weights:

$$\begin{pmatrix} w_1 \\ w_2 \\ \vdots \\ w_N \\ w_{N+1} \end{pmatrix} = \begin{pmatrix} 1 & \cdots & 1 & 1 \\ \cos 2\theta_1 & \cdots & \cos 2\theta_N & \cos 2\theta_{N+1} \\ \cos 4\theta_1 & \cdots & \cos 4\theta_N & \cos 4\theta_{N+1} \\ \vdots & & \vdots & \vdots \\ \cos 2N\theta_1 & \cdots & \cos 2N\theta_N & \cos 2N\theta_{N+1} \end{pmatrix}^{-1} \cdot \begin{pmatrix} 1 \\ -\frac{1}{3} \\ -\frac{1}{15} \\ \vdots \\ \frac{-1}{4N^2-1} \end{pmatrix} \tag{2.26}$$

Due to symmetry the weights are just mirrored for the other hemisphere:

$$w_i = w_{2(N+1)-i+1}, \quad i = 1, \cdots, N+1 \tag{2.27}$$

We may define a vector $\boldsymbol{w} = [w_1, w_2, \cdots, w_J]^T$ containing the quadrature weights for the J latitude circles. To correspond the current matrix notation, $\boldsymbol{w}$ needs to be repeated J times for each meridian, and stored in a diagonal matrix. With an additional normalization constant[1] we define the quadrature-weight matrix as:

$$\boldsymbol{W} = \frac{2\pi}{N+1} \operatorname{diag}\{[\underbrace{\boldsymbol{w}^T, \cdots, \boldsymbol{w}^T}_{\times J}]\} \tag{2.28}$$

The re-established orthogonality for a matrix $\boldsymbol{C}_{SH,N}$, cf. Eq.(2.10), is stated as:

$$\boldsymbol{C}_{SH,N}^T \boldsymbol{W} \boldsymbol{C}_{SH,N} = \boldsymbol{I} \tag{2.29}$$

Hence the pseudo inverse in Eq.(2.16) can be replaced by $\boldsymbol{C}_{SH,N}^T \boldsymbol{W}$ and no matrix inversion is needed:

$$\chi_{SH,N} = \boldsymbol{C}_{SH,N}^T \boldsymbol{W} \boldsymbol{x} \tag{2.30}$$

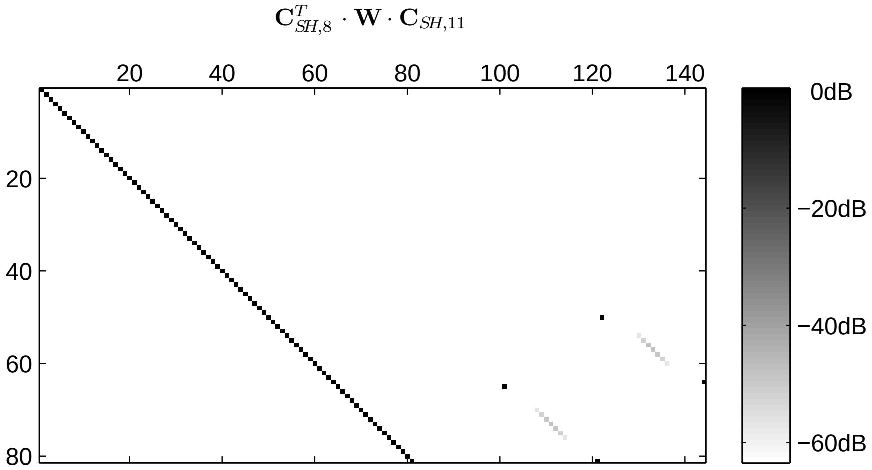

(a) quadrature weights

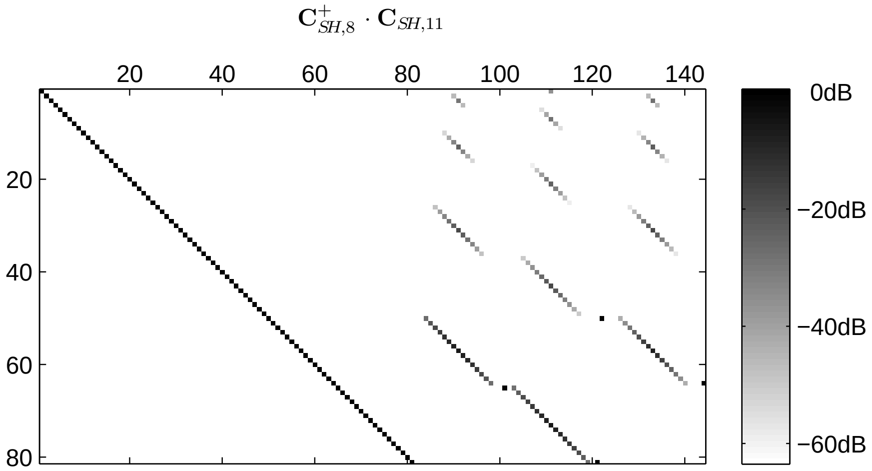

(b) pseudo inverse

Figure 8: Aliasing error due to a pattern of order 11 sampled by an equiangular grid with 324 sampling points

To give an illustrative example for comparison of quadrature weights and pseudo inverse, we assume an equiangular sample layout having $K = 324$ sampling points, fulfilling the spatial sampling theorem up to an order $N = 8$. An input pattern $\boldsymbol{x}$ to be analyzed is assumed to be band-limited with order $\tilde{N} = 11$ to evoke aliasing. Figure 8 depicts the matrix according to the aliasing error in Eq.(2.21) for a) applying quadrature weights and b) using the pseudo inverse. It is seen that approaches establish an identity matrix on the left side and thus will determine exactly the Fourier coefficients of patterns being band-limited on the sphere with maximum order $N = 3$. The non-zero entries on the right side of the matrix products show that the spread of aliasing error is

---

[1] Note that the scaling constant $\frac{N+1}{2\pi}$ results from the discrete Fourier transform.

quite different for the two approaches and in this context the quadrature weights show a preferable behavior.

2.6.2 Equal Angular Resolution Grid

For the measurements in section 2.2 an intuitive grid layout was chosen with $\Delta\varphi = \Delta\theta$. Since this layout provides a equal angle resolution[1] in longitude and latitude and the term *equiangular* is already occupied, we will refer to it as the *equal angular resolution* grid (hereafter EAR grid).

In comparison with the equiangular grid, the EAR grid has twice as much meridians as longitude circles. With J being the number of sampling points on a meridian, the number of samples on the sphere is $K = 2J^2$. According to Eq.(2.24), the angular position vector $\boldsymbol{\theta}_k$ of a grid-node k is determined for a EAR layout symmetric to the equator by:

$$\boldsymbol{\theta}_k = \left[\frac{\pi}{J} \cdot \operatorname{div}(k, J) \ , \ \frac{\pi}{J} \cdot \left(\operatorname{mod}(k, J) + \frac{1}{2} \right) \right], \qquad k = 0, 1, \cdots, K-1 \tag{2.31}$$

The condition number $\kappa\left(\boldsymbol{C}_{SH,N}^T \boldsymbol{C}_{SH,N}\right)$ is crucial for calculating the pseudo inverse $\boldsymbol{C}_{SH,N}^{+}$, since it reveals the accuracy of the matrix inversion in Eq.(2.16) and determines the maximum order up to which the spatial sampling theorem is fulfilled. It has turned out, that for a comparable number of sample points the EAR grid satisfies the sampling condition up to higher orders than an equiangular layout. As an example, Figure 9 depicts $\kappa\left(\boldsymbol{C}_{SH,N}^T \boldsymbol{C}_{SH,N}\right)$ as a function of the order N for an equiangular and an EAR configuration with a comparable number of samples. It is seen that for the equiangular grid with $K = 676$ the condition number skyrockets for $N > 12$, what is consistent with Eq.(2.22) and shows that in this case the pseudo inverse does not lead to a higher analysis order than the quadrature weights. However, the condition number of the EAR grid with $K = 648$ does not escalate until $N = 17$ and thus allows up to this order an aliasing free estimation of the Fourier coefficient with even less samples.

As an improvement to the pseudo inverse in Eq.(2.18), let us consider a weighted pseudo inverse using a weighted least squares approach. So we insert a diagonal matrix

---

[1] This is similar to the equidistant cylindrical projection (ECB), cf. Muciaccia [MNV97].

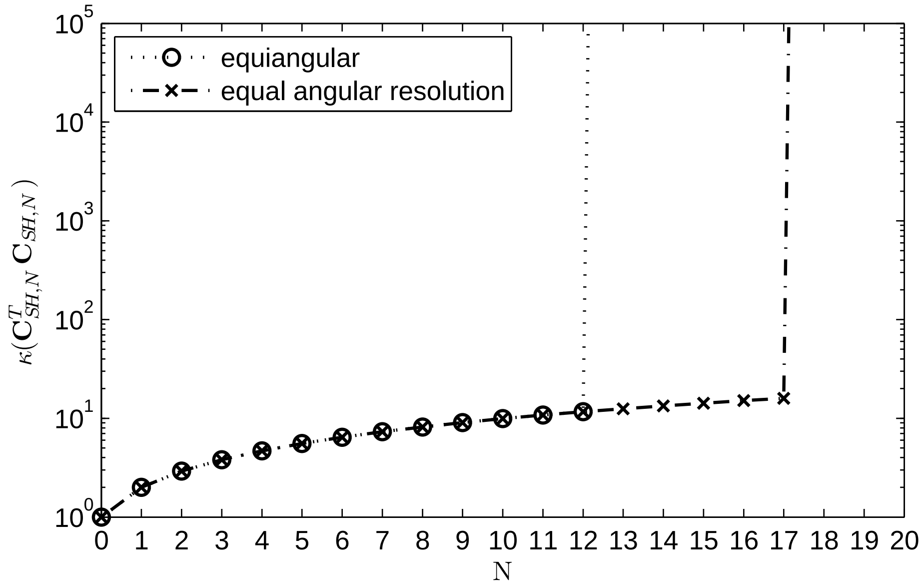

Figure 9: Crucial condition number of the pseudo inverse for an equiangular layout with $K = 676$ and an EAR layout with $K = 648$

$\boldsymbol{W}^{\frac{1}{2}} = \operatorname{diag}\left\{\sqrt{w_0}, \cdots, \sqrt{w_K}\right\}$ in Eq.(2.13), which weights the components of the error vector due to their importance:

$$\min_{\chi_{SH,N}} \left\| \boldsymbol{W}^{\frac{1}{2}}(\boldsymbol{x} - \boldsymbol{C}_{SH,N}\boldsymbol{\chi}_{SH,N}) \right\|_2^2 \tag{2.32}$$

Thus the weighted squared error norm is determined by

$$\begin{aligned}(\boldsymbol{x} - \boldsymbol{C}_{SH,N}\boldsymbol{\chi}_{SH,N})^T \boldsymbol{W} (\boldsymbol{x} - \boldsymbol{C}_{SH,N}\boldsymbol{\chi}_{SH,N}) &= \\ \boldsymbol{x}\boldsymbol{W}\boldsymbol{x}^T - \boldsymbol{\chi}_{SH,N}^T \boldsymbol{C}_{SH,N}^T \boldsymbol{W}\boldsymbol{x} - \boldsymbol{x}^T \boldsymbol{W}\boldsymbol{C}_{SH,N}\boldsymbol{\chi}_{SH,N} + \boldsymbol{\chi}_{SH,N}^T \boldsymbol{C}_{SH,N}^T \boldsymbol{W}\boldsymbol{C}_{SH,N}\boldsymbol{\chi}_{SH,N}\end{aligned} \tag{2.33}$$

an differentiating w.r.t $\boldsymbol{\chi}_{SH,N}^T$ and setting the result equal zero leads to:

$$\boldsymbol{\chi}_{SH,N} = \left(\boldsymbol{C}_{SH,N}^T \boldsymbol{W}\boldsymbol{C}_{SH,N}\right)^{-1} \boldsymbol{C}_{SH,N}^T \boldsymbol{W}\boldsymbol{x} \tag{2.34}$$

Since an ideal sampling is distributed uniformly over the sphere, intuitively the wider spaced samples near the equator are more important than the denser samples near the poles. So from a geometrical point of view, it stands to reason to weight the sampling points according to the equivalent surface fraction they are representing. The surface S_{sl} of a sphere slice bounded by $\theta_i < \theta < \theta_j$, as a fraction of the entire sphere surface with equal radius, is calculated by:

$$\frac{S_{sl}}{4\pi r^2} = \frac{\cos\theta_i - \cos\theta_j}{2} \tag{2.35}$$

For our grid, the sphere slice according to a latitude circle of node points is bounded by $\left(\theta_l - \frac{\pi}{2J}\right) < \theta < \left(\theta_l + \frac{\pi}{2J}\right)$, where θ_l is the elevation of the latitude circle. For an equal angular resolution grid, we have $2J$ equiangular spaced node points on each latitude circle. So the equivalent surface fraction S_k of a node point on the latitude circle at θ_l as a fraction of the entire sphere surface yields:

$$\frac{S_k}{4\pi r^2} = \frac{S_{sl}}{2J} = \frac{\cos\theta_k - \cos\theta_k}{4J} \tag{2.36}$$

With Eq.(2.36), the weight for each sampling point according to the its equivalent surface fraction can be combined to a diagonal weight matrix:

$$\boldsymbol{W}_{sf} = \operatorname{diag}\left\{\left[\frac{\cos\theta_0 - \cos\theta_0}{4J}, \cdots, \frac{\cos\theta_K - \cos\theta_K}{4J}\right]\right\} \tag{2.37}$$

It turns out, that the weights due to the surface fraction are very similar in appearance to the quadrature weights of an equiangular grid with equal latitude circles. Figure 10 depicts the condition number $\kappa\left(\boldsymbol{C}_{SH,N}^T \boldsymbol{W} \boldsymbol{C}_{SH,N}\right)$ for an EAR grid with $K = 648$, like used for the measurements in section 2.2, as a function of order N for different choices of the weight matrix $\boldsymbol{W}$. The equal sample weighting refers to unweighted pseudo inverse, thus the condition number is the same as in Figure 9 and just plotted for comparison. The weighting due to the associated surface fractions yields a noticeable enhancement of the condition of $\boldsymbol{C}_{SH,N}^T \boldsymbol{W} \boldsymbol{C}_{SH,N}$ and thus leads to a more accurate calculation of the pseudo inverse. However, the quadrature weights seem to the best choice, providing an even lower condition number.

2.7 Control by System Inversion

Recall that the aim is to design a control unit, that is capable of reproducing spherical harmonic base functions at the measurement surface with the icosahedral loudspeaker array. Consequently the control system describes a mapping of the individual spherical harmonic coefficient to frequency domain weights at the transducers, such that the sound pressure at the measurement grid corresponds to the respective base function.

To do so, the sound pressure in Eq.(2.1) is transformed into the spherical harmonics domain. Certainly this may not be a strictly a band-limited function on the sphere, but

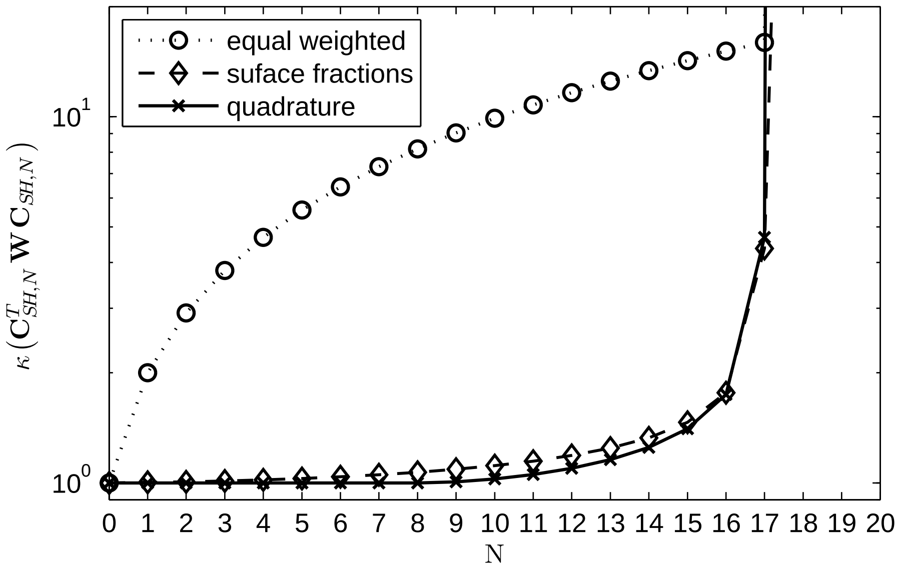

Figure 10: Crucial condition number of the weighted pseudo inverse for an EAR layout with $K = 648$

we assume that the aliasing error caused by harmonics of higher order than the analysis order N_a [1] is negligibly low. A left multiplication with the analysis matrix developed in section 2.6 accpomplishes transformation:

$$\boldsymbol{\psi}_{SH,N_a} = \underbrace{\boldsymbol{C}^{+}_{SH,N_a}\,\boldsymbol{G}}_{\overset{c}{\boldsymbol{G}}_{SH,N_a}}\,\boldsymbol{u} \tag{2.38}$$

where $\boldsymbol{\psi}_{SH,N_a} = \mathrm{vec}_{SH,N_a}\,\{\psi_n^m\}$ is the spherical harmonics coefficients vector of the sound pressure and $\overset{c}{\boldsymbol{G}}_{SH,N_a}$ the system matrix of the transformed[2] MIMO-system mapping the loudspeaker excitation signals onto spherical harmonics coefficients.

A proper inversion of Eq. (2.38) is required to determine an excitation vector $\boldsymbol{u}$ which synthesizes a directivity pattern with specified Fourier coefficients. From the spatial sampling theorem we know that the icosahedral array, equipped with $L = 20$ loudspeakers, is limited by a maximum synthesis order $N_c = 3$. Defining a steering vector $\boldsymbol{\gamma}_{SH,N_c}$, containing the $(N_c + 1)^2$ coefficients of the desired pattern, and an $L \times (N_c + 1)^2$ matrix $\overset{\circ}{\boldsymbol{B}}$ representing the control unit, mapping the spherical harmonics onto

---

[1] Note that in the following it has to be distinguished between the maximum controllable order of the loudspeaker array and the maximum order up to which the microphone array provides an aliasing free estimation of the Fourier coefficients, thus the former will be denoted hereafter by N_c and the latter by N_a.

[2] The superscript of $\overset{c}{\boldsymbol{G}}$ indicates that only the left side of the matrix is in the spherical harmonics domain. In a letter section a matrix $\overset{\circ}{\boldsymbol{G}}$ will be introduced, for which the right hand side was also transformed. The latter represents the system matrix in the spherical harmonics domain.

the loudspeaker signals $\boldsymbol{u}$, the desired control unit yields:

$$\boldsymbol{u} = \overset{\supset}{\boldsymbol{B}}\, \boldsymbol{\gamma}_{SH,N_c} \tag{2.39}$$

And the over all system equation reads as follows:

$$\boldsymbol{\psi}_{SH,N_a} = \boldsymbol{C}_{SH,N_a}\, \boldsymbol{G}\, \overset{\supset}{\boldsymbol{B}}\, \boldsymbol{\gamma}_{SH,N_c} \tag{2.40}$$

Assume an ideal control unit $\overset{\supset}{\boldsymbol{B}}_{\mathrm{opt}}$, that produces exactly the desired pattern at the measurement sphere, so that:

$$\begin{bmatrix} \boldsymbol{\gamma}_{SH,N_c} \\ 0 \\ \vdots \\ 0 \end{bmatrix} = \overset{\text{c}}{\boldsymbol{G}}_{SH,N_a}\, \overset{\supset}{\boldsymbol{B}}_{\mathrm{opt}}\, \boldsymbol{\gamma}_{SH,N_c} \tag{2.41}$$

it is seen that $\overset{\supset}{\boldsymbol{B}}_{\mathrm{opt}}$ has to be right inverse to $\overset{\text{c}}{\boldsymbol{G}}_{SH,N_a}$. Since Eq. (2.38) represents a overdetermined system, it has no exact solution. Thus the remaining alternatives are to reduce the constraints or to solve it approximately. In the following these possibilities are discussed and the error arising from the different approaches is compared.

2.7.1 Exact Inversion in the Array Achievable Subspace

The maximum spherical harmonics order order the icosahedral array is capable to synthesize is limited with $N_c = 3$. Accordingly we may truncate Eq. (2.38) so that only spherical harmonics up to order N_c are considered:

$$\boldsymbol{\psi}_{SH,N_c} = \overset{\text{c}}{\boldsymbol{G}}_{SH,N_c}\, \boldsymbol{u} \tag{2.42}$$

The truncated system matrix $\overset{\text{c}}{\boldsymbol{G}}_{SH,N_c}$ is exactly right invertible due to the fact that its row rank is higher than its column rank. For this class of matrices, the pseudo inverse is the right inverse which is calculated by:

$$\overset{\text{c}}{\boldsymbol{G}}{}^{+}_{SH,N_c} = \overset{\text{c}}{\boldsymbol{G}}{}^{T}_{SH,N_c} \left(\overset{\text{c}}{\boldsymbol{G}}_{SH,N_c} \overset{\text{c}}{\boldsymbol{G}}{}^{T}_{SH,N_c} \right)^{-1} \tag{2.43}$$

Using $\overset{\text{c}}{\boldsymbol{G}}^{+}_{SH,N_c} = \left(\boldsymbol{C}^{+}_{SH,N_c}\boldsymbol{G}\right)^{+}$ as approximate control system $\overset{\text{ɔ}}{\boldsymbol{B}}$, the overall system according to Eq. (2.40) reads as:

$$\boldsymbol{\psi}_{SH,N_a} = \underbrace{\overset{\text{c}}{\boldsymbol{G}}_{SH,N_a}\overset{\text{c}}{\boldsymbol{G}}^{+}_{SH,N_c}}_{\begin{bmatrix}\boldsymbol{I}_{SH,N_c}\\ \\ \boldsymbol{?}_{SH,N_c\rightarrow N_a}\end{bmatrix}}\boldsymbol{\gamma}_{SH,N_c} \tag{2.44}$$

In a similar way as in Eq. (2.21), it can be shown that the pseudo-inverse yields an exact solution within the truncated spherical harmonics subspace. In addition, the uncontrolled subspace expressed as $\boldsymbol{?}_{SH,N_c\rightarrow N_a}$ is present, due to spatial aliasing caused by the sampling of the loudspeaker array. Since this subspace may contain non-zero elements, higher-order spherical harmonics are produced which corrupt the synthesized pattern.

2.7.2 Approximate Inversion Considering Higher Order Harmonics

Alternatively to the inversion in the reduced subspace with the the maximum synthesis order N_c, it seems more promising to regard also the higher order harmonics up to the analysis order N_a. However, this leads to an overdetermined system having more constraints than unknowns. Thus only an approximate solution in a least squares sense can be determined for Eq.(2.38):

$$\min_{\boldsymbol{u}} \left\| \boldsymbol{\psi}_{SH,N_a} - \overset{\text{c}}{\boldsymbol{G}}_{SH,N_a}\boldsymbol{u} \right\|_2^2 \tag{2.45}$$

The solution of this minimization problem is derived similarly as in Eqs.(2.14) and (2.15), leads again to the pseudoinverse $\overset{\text{c}}{\boldsymbol{G}}^{+}_{SH,N_a}$. But in this case it is the left inverse. Solving Eq.(2.38) yields:

$$\hat{\boldsymbol{u}} = \overset{\text{c}}{\boldsymbol{G}}^{+}_{SH,N_a} \cdot \begin{bmatrix}\boldsymbol{\gamma}_{SH,N_c}\\ 0\\ \vdots\\ 0\end{bmatrix} \tag{2.46}$$

where $\hat{\boldsymbol{u}}$ yields the best approximation due to Eq.(2.45). It is seen form the above equation that only the $(N+1)^2$ columns left in $\overset{\text{c}}{\boldsymbol{G}}^{+}_{SH,N_a}$ are needed to determine $\hat{\boldsymbol{u}}$, and we define a matrix only containing the relevant columns by $\left(\overset{\text{c}}{\boldsymbol{G}}^{+}_{SH,N_a}\right)_{SH,N_c}$. Using $\left(\overset{\text{c}}{\boldsymbol{G}}^{+}_{SH,N_a}\right)_{SH,N_c}$

as control unit in Eq. (2.40), the squared error is minimized for all spherical harmonics up to the analysis order N_a, and the overall system results in:

$$\boldsymbol{\psi}_{SH,N_a} = \underbrace{\overset{\text{c}}{\boldsymbol{G}}_{SH,N_a} \left(\overset{\text{c}}{\boldsymbol{G}}^{+}_{SH,N_a}\right)_{SH,N_c}}_{\begin{bmatrix} \approx \boldsymbol{I}_{SH,N_c} \\ \approx \mathbf{0}_{SH,N_c \to N_a} \end{bmatrix}} \boldsymbol{\gamma}_{SH,N_c} \tag{2.47}$$

With $\approx \boldsymbol{I}_{SH,N_c}$ and $\approx \mathbf{0}_{SH,N_c \to N_a}$ it should be indicated that the least-squares approximation is the best achievable trade-off between exact control of spherical harmonics up to N_c and an all-zero matrix for higher order harmonics. That means complete control over the N_c-subspace is given up by virtue of spatial aliasing suppression. A more detailed analysis of the error will be given in a later section.

2.7.3 System Inversion in the Spherical Harmonics Domain

As already stated, the icosahedral array is capable of pattern synthesis up to an order $N_c = 3$, represented by 16 spherical harmonic base functions. The degrees of freedom of a loudspeaker array are related to the number of transducer. The icosahedral array with its 20 loudspeakers has more degrees of freedom than required for order $N_c = 3$. This fact can be exploited to reduce the size of the control unit and thus the computational cost. As shown in the following, this is done by introducing a decoder matrix.

Decoder: Let us assume a continuous driving voltage distribution $u(\boldsymbol{\theta})$ as the sum of Dirac delta functions located at the center of each loudspeaker and weighted by the according excitation signals:

$$u(\boldsymbol{\theta}) = \sum_{l=1}^{L} \delta(\boldsymbol{\theta} - \boldsymbol{\theta}_l) \cdot u^{(l)} \tag{2.48}$$

The Fourier coefficients Υ_{nm} of this distribution can be determined according to Eq. (2.4):

$$\begin{aligned} \Upsilon_{nm} &= \int_{\Omega} \sum_{l=1}^{L} \delta(\boldsymbol{\theta} - \boldsymbol{\theta}_l)\, u^{(l)} Y_n^m(\boldsymbol{\theta}) d\Omega \\ &= \sum_{l=1}^{L} \int_{\Omega} \delta(\boldsymbol{\theta} - \boldsymbol{\theta}_l) Y_n^m(\boldsymbol{\theta}) d\Omega\, u^{(l)} \\ &= \sum_{l=1}^{L} Y_{nm}(\boldsymbol{\theta}_l) \cdot u^{(l)} \end{aligned} \tag{2.49}$$

With the following definitions:

$$\boldsymbol{\Upsilon}_{SH} = \mathrm{vec}_{SH}\left\{\Upsilon_{nm}\right\}, \qquad \boldsymbol{D}_{SH} = \left[\mathrm{vec}_{SH}\left\{Y_{nm}(\boldsymbol{\theta}_1)\right\}, \mathrm{vec}_{SH}\left\{Y_{nm}(\boldsymbol{\theta}_2)\right\}, \cdots, \mathrm{vec}_{SH}\left\{Y_{nm}(\boldsymbol{\theta}_L)\right\}\right]$$

Eq. (2.49) can be expressed as a matrix equation:

$$\boldsymbol{\Upsilon}_{SH} = \boldsymbol{D}_{SH}\,\boldsymbol{u} \tag{2.50}$$

Assuming the system is band-limited on the sphere with maximum order N_c and replacing $\boldsymbol{\Upsilon}_{SH,N_c}$ by the steering vector $\boldsymbol{\gamma}_{SH,N_c}$ yields:

$$\boldsymbol{\gamma}_{SH,N_c} = \boldsymbol{D}_{SH,N_c}\,\boldsymbol{u} \tag{2.51}$$

Finally, the driving voltages can be determined by applying the pseudo inverse:

$$\boldsymbol{u} = \boldsymbol{D}^{+}_{SH,N_c}\,\boldsymbol{\gamma}_{SH,N_c} \tag{2.52}$$

Since $\boldsymbol{D}^{+}_{SH,N_c}$ provides a sensible mapping of the steering vector onto the transducer excitation signals, it will be referred to as the decoder matrix.

MIMO-System in the Spherical Harmonic Domain: Inserting the decoder from Eq.(2.52) into Eq.(2.38) we get:

$$\boldsymbol{\psi}_{SH,N_a} = \underbrace{\boldsymbol{C}_{SH,N_a}\,\boldsymbol{G}\,\boldsymbol{D}^{+}_{SH,N_c}}_{\mathring{\boldsymbol{G}}_{SH,N_a}}\,\boldsymbol{\gamma}_{SH,N_c} \tag{2.53}$$

The resulting system matrix $\mathring{\boldsymbol{G}}_{SH,N_a}$ can be interpreted as a spherical harmonics domain representation of the MIMO-system in Figure 3, since it characterizes the transmission of spherical harmonics coefficients all the way from the encoded input to the measurement surface. We introduce a control system in the spherical harmonics domain denoted by $\mathring{\boldsymbol{B}}$, which ideally should be right inverse to $\mathring{\boldsymbol{G}}_{SH,N_a}$:

$$\begin{aligned}\boldsymbol{\psi}_{SH,N_a} &= \mathring{\boldsymbol{G}}_{SH,N_a}\,\mathring{\boldsymbol{B}}\,\boldsymbol{\gamma}_{SH,N_c}\\ &= \boldsymbol{C}_{SH,N_a}\,\boldsymbol{G}\,\underbrace{\boldsymbol{D}^{+}_{SH,N_c}\,\mathring{\boldsymbol{B}}}_{\mathring{\boldsymbol{B}}}\,\boldsymbol{\gamma}_{SH,N_c}\end{aligned} \tag{2.54}$$

From the above equation it is clear that the real-world control unit $\mathring{\boldsymbol{B}}$ consists of the frequency independent decoder and a spherical harmonics control unit.

System Inversion: For the system inversion in the spherical harmonics domain, the same considerations as in subsections 2.7.1 and 2.7.2 can be made. So again the inversion of Eq. (2.53) can be either done exact in a reduced subspace, or an approximate solution can be determined in a least squares sense. In the former case, truncating the system by N_c, $\mathring{\boldsymbol{G}}_{SH,N_c}$ becomes a $(N_c + 1)^2 \times (N_c + 1)^2$ square matrix and the control system in the spherical harmonics domain can be set to:

$$\mathring{\boldsymbol{B}} = \left(\boldsymbol{C}_{SH,N_c}\, \boldsymbol{G} \boldsymbol{D}^{+}_{SH,N_c}\right)^{-1} \tag{2.55}$$

The second approach, the approximate inversion considering higher order harmonics, is provided by the pseudo inverse $\mathring{\boldsymbol{G}}^{+}_{SH,N_a}$, where again only only the left $(N_c + 1)^2$ columns are needed, cf. Eq. (2.46), so that the control system in the spherical harmonics domain can be set to:

$$\mathring{\boldsymbol{B}} = \left(\boldsymbol{C}_{SH,N_a}\, \boldsymbol{G}\, \boldsymbol{D}^{+}_{SH,N_c}\right)^{+}_{SH,N_c} \tag{2.56}$$

It is seen that in both cases $\mathring{\boldsymbol{B}}$ is a $(N_c + 1)^2 \times (N_c + 1)^2$ matrix. So compared to sections 2.7.2 and 2.7.1 the size of the frequency dependent matrix in the control unit for the icosahedral array is reduced from 20×20 to 16×16 by introducing a frequency independent decoder matrix.

2.8 Simulation Results

In the following will demonstrate the control unit developed in the previous section using the measured data of the IEM icosahedral loudspeaker array. The system inversion is done in in the spherical harmonics domain using the decoder matrix. The first example shows how the spherical harmonics base functions are reproduced by the array and in the second example a beam pattern is considered.

Spherical Harmonics Base Functions: The 16 base functions up to order 3 as reproduced by the icosahedral array are depicted in Figure 11 for three selected third-octave bands with center frequencies a) 79Hz, b) 503Hz and c) 799Hz. For this example the control unit was determined by system inversion in the N_c-truncated subspace. Comparing these patterns with the analytic functions, cf. Figure 7, it is seen that the approximation for low frequencies is quite good, but for higher frequencies the patterns are corrupted by higher order harmonics due to the spatial aliasing of the loudspeaker array.

Beam Pattern As an example for a composite pattern a band-limited beam pattern with maximum order 3 is considered. Figure 12 shows the beam pattern produced by the loudspeaker array for several third-octave bands. Thereby in a) the system inversion is done within the subspace up to order $N_c = 3$, whereas in b) the higher order harmonics up to order $N_a = 17$ are considered for system inversion. Comparing sub-figure a) and b) it is seen that for low frequencies, where no spatial aliasing occurs, both approaches achieve comparable good results. For higher frequencies where spatial aliasing is present, the approaches show a quiet different behavior. Since system inversion in the N_c-truncated subspace does not consider the higher order harmonics, components emerging from spatial aliasing of the loudspeaker array are added to the desired spherical harmonics and corrupt the pattern. From sub-figure b) it is seen that considering the higher order harmonics in the inversion leads to a different result. Minimizing the approximation error in a least squares sense suppresses higher order harmonics due to aliasing, but also the desired spherical harmonics up to order N_c are affected.

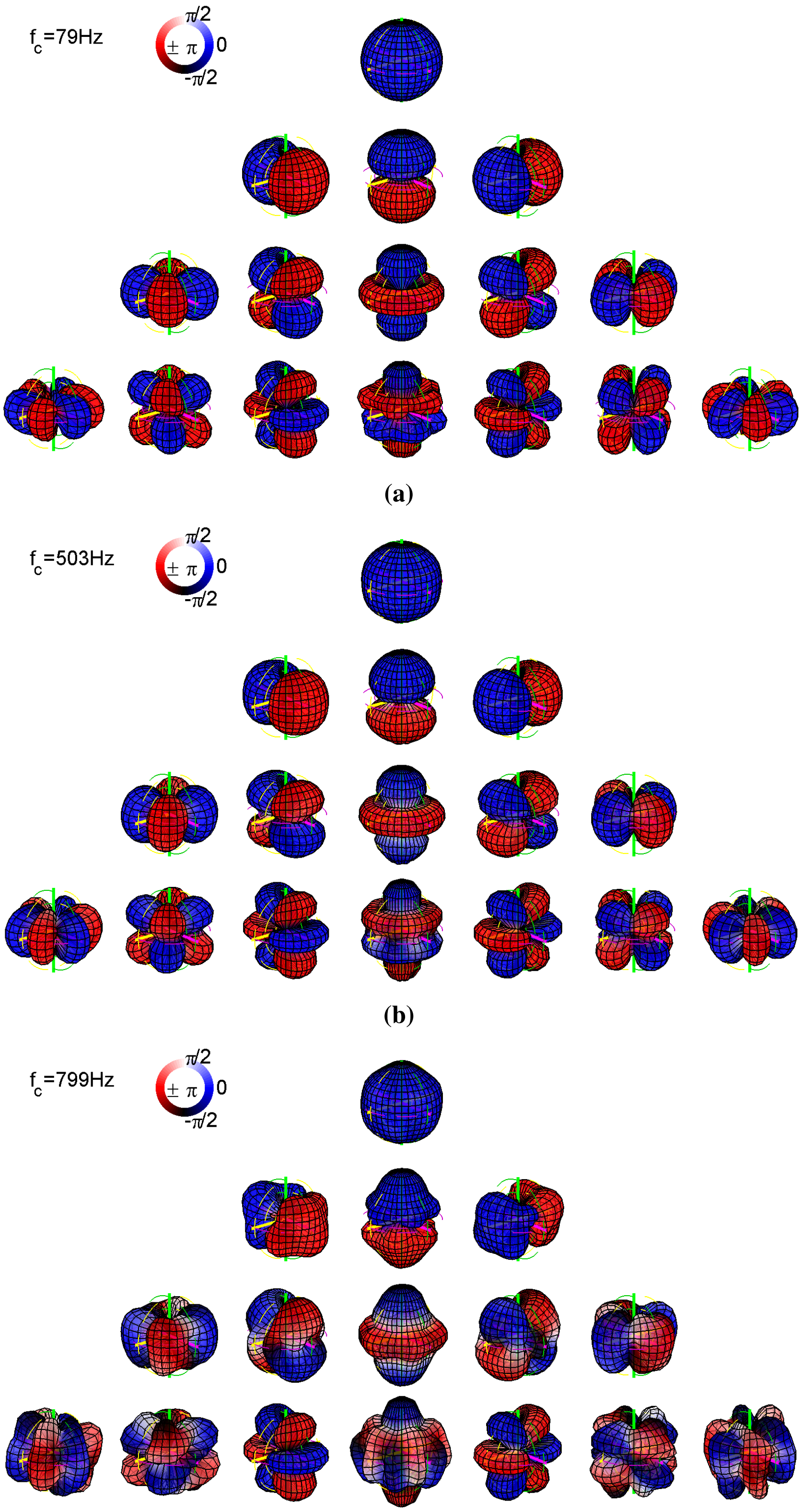

(a)

(b)

(c)

Figure 11: Spherical harmonics base functions approximated by the IEM icosahedral loudspeaker array for three selected third-octave bands.

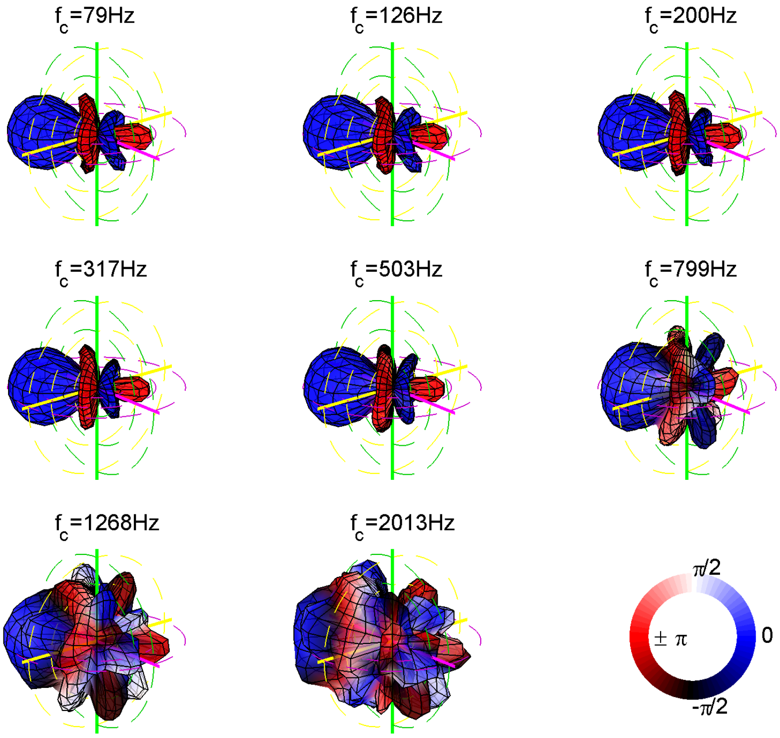

(a) Beam pattern using an N_c-subspace control unit

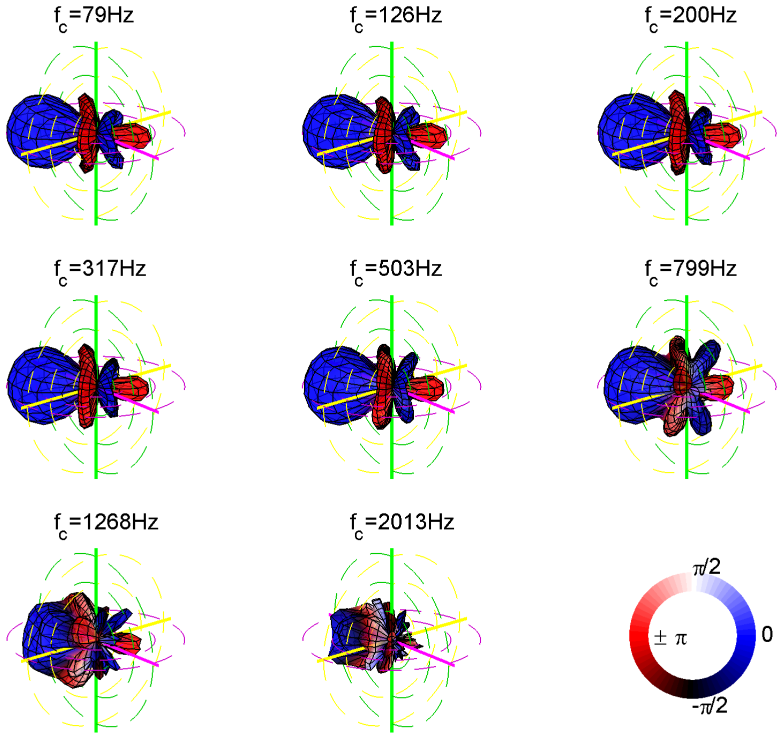

(b) Beam pattern using approximate system inversion considering harmonics up to N_a

Figure 12: Band-limited beam patterns with N=3 approximated by the IEM icosahedral loudspeaker array for several third-octave bands.

2.9 Error Analysis

This subsection will have a closer look on the error due to system inversion for both approaches discussed in section 2.7.

Error Vector, Error Matrix: Let us define an error vector $\boldsymbol{e}$, representing the deviation of the desired pattern from the one established at the measurement sphere, in terms of spherical harmonics coefficients:

$$\boldsymbol{e}(\boldsymbol{\gamma}_{SH,N_c}) = \boldsymbol{\psi}_{SH,N_a} - \begin{bmatrix} \boldsymbol{\gamma}_{SH,N_c} \\ 0 \\ \vdots \\ 0 \end{bmatrix} \tag{2.57}$$

Substituting $\boldsymbol{\psi}_{SH,N_a}$ according to Eq.(2.40) yields:

$$\boldsymbol{e}(\boldsymbol{\gamma}_{SH,N_c}) = \underbrace{\left(\boldsymbol{C}_{SH,N_a} \boldsymbol{G} \mathring{\boldsymbol{B}} - \begin{bmatrix} \boldsymbol{I}_{SH,N_c} \\ \boldsymbol{0}_{SH,N_c \to N_a} \end{bmatrix} \right)}_{\boldsymbol{E}} \cdot \boldsymbol{\gamma}_{SH,N_c} \tag{2.58}$$

where the term in parenthesis is interpreted as a generalized error matrix $\boldsymbol{E}$, representing the deviation of the overall system matrix from the desired one. The error-matrix can determined for arbitrary control systems by substituting the control matrix $\mathring{\boldsymbol{B}}$ accordingly. It is seen that multiplying the error matrix with an arbitrary steering vector yields the associated error vector. The squared euclidean norm of the error vector represents the error power and thus is an appropriate reference value to evaluate the accuracy of an approximated pattern. According to Zotter [Zot], the squared error norm can be determined for any steering vector from the error matrix by:

$$||\boldsymbol{e}||_2^2 = \boldsymbol{\gamma}_{SH,N_c}^T \boldsymbol{E}^T \boldsymbol{E} \boldsymbol{\gamma}_{SH,N_c} \tag{2.59}$$

Comparison of the Exact System Inversion the Approximate Inversion: From Eq.(2.58) can be seen that the ideal error-free overall system matrix would consist of an $(N_c+1)^2 \times (N_c+1)^2$ upper identity matrix and a lower $\left((N_a+1)^2 - (N_c+1)^2\right) \times (N_c+1)^2$ all-zero matrix. Accordingly, the error-matrix can be split in two parts, namely an upper matrix $\boldsymbol{E}_{SH,N_c}$ due to the error in the N_c-subspace and a lower matrix $\boldsymbol{E}_{SH,N_c\rightarrow N_a}$ caused by the presence of higher order harmonics due to spatial aliasing of the spherical loudspeaker array:

$$\boldsymbol{E} = \begin{bmatrix} \boldsymbol{E}_{SH,N_c} \\ \boldsymbol{E}_{SH,N_a\rightarrow N_c} \end{bmatrix} \tag{2.60}$$

Analogously, the error vector $\boldsymbol{e}$ can be split in an error vector for the N_c-truncated subspace

$$\boldsymbol{e}_{SH,N_c} = \boldsymbol{E}_{SH,N_c} \cdot \boldsymbol{\gamma} \tag{2.61}$$

and an error vector for the higher order harmonics:

$$\boldsymbol{e}_{SH,N_c\rightarrow N_a} = \boldsymbol{E}_{SH,N_c\rightarrow N_a} \cdot \boldsymbol{\gamma} \tag{2.62}$$

The system inversion in the array achievable subspace is exact and thus yields a vanishing $\boldsymbol{E}_{N_c}$ and the error is only caused by higher order components, i.e. the result of spatial aliasing in the transducer array. This means that just the 2-norm of the order-truncated error vector $\boldsymbol{e}_{N_c}$ is minimized.

Approximate inversion also takes higher order harmonics into account. Let us first assume the hypothetic case that no higher order harmonics are present, i.e. $\boldsymbol{E}_{SH,N_c\rightarrow N_a} = \boldsymbol{0}_{SH,N_c\rightarrow N_a}$. Consequently, $\left\|\boldsymbol{e}_{SH,N_c\rightarrow N_a}\right\|_2 = 0$ and thus the minimization of the error vector norm $||\boldsymbol{e}||_2$ leads to the same result as the exact inversion in the N_c-truncated subspace. But if higher order harmonics due to spatial aliasing are present, the approximate approach finds the best achievable trade-off between a low approximation error of the desired harmonics $\left\|\boldsymbol{e}_{SH,N_c}\right\|_2$ and a suppression of the unwanted higher order harmonics, so that $\left\|\boldsymbol{e}_{SH,N_c\rightarrow N_a}\right\|_2 \overset{!}{=} 0$. This behavior can be interpreted as a kind of spatial anti-aliasing filter. On the other hand, if aliasing dominates the whole frequency domain, approximate system inversion leads to no output at all.

Error Bounds: Since the product $\boldsymbol{E}^T\boldsymbol{E}$ is a symmetric matrix, its eigendecomposition leads to (cf. [Zot]):

$$\boldsymbol{E}^T\boldsymbol{E} = \boldsymbol{Q} \cdot \mathrm{diag}\{\sigma_e\}^2 \cdot \boldsymbol{Q}^T \tag{2.63}$$

where $\sigma^2_{e,nm}$ are the eigenvalues and $\boldsymbol{Q}$ is a matrix containing the corresponding eigenvectors.

Let us assume the norm of the target patterns is normalized to unity, such that $\left\|\boldsymbol{\gamma}_{SH,N_c}\right\|_2 = 1$. From Eqs.(2.58) and (2.63) it follows that the smallest achievable error power is given by $\min(\sigma_{e,nm})$ and the related directivity pattern is determined by the associated eigenvector. Analogously, the largest error power is given by $\max(\sigma_{e,nm})$ related to the directivity pattern determined by the corresponding eigenvector. So a frequency dependent upper and lower error bound results from the eigendecompositon for arbitrary unity gain target patterns. This bounds are shown in Figure 13, where the solid lines depict the error bounds for the the exact inversion in the N_c-subspace and the dashed lines depict the error bounds for the the approximated inversion considering higher order harmonics. Subfigure (a) depicts the error bounds for target patterns up to order 3 and in (b), (c) and (d) the maximum pattern order is stepwise reduced. It can be seen, that the error increases for higher frequencies due to spatial aliasing and the gap between the upper and the lower bound decreases. In contrast to the exact inversion in the N_c-subspace the approximate inversion limits the error to 0dB.

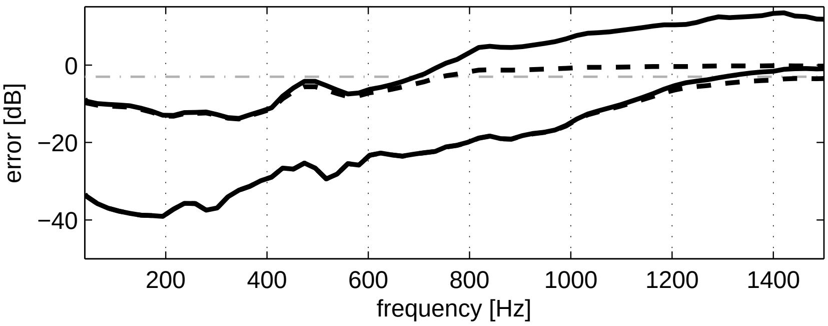

(a) N=3

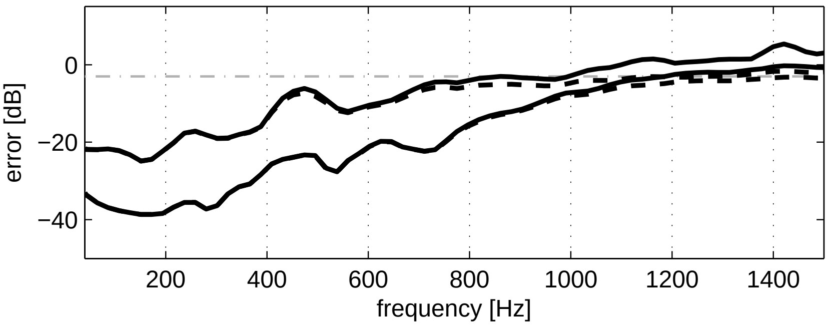

(b) N=2

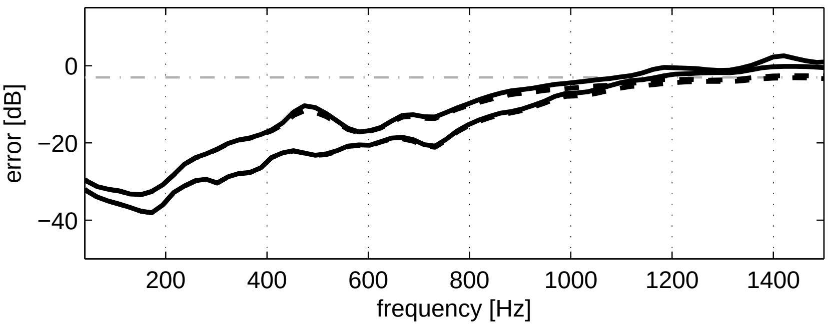

(c) N=1

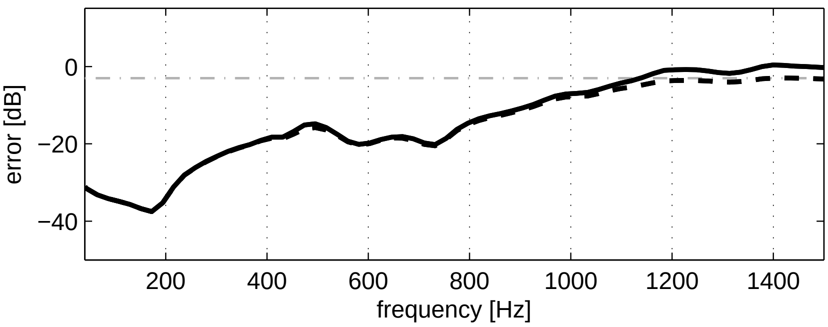

(d) N=0

Figure 13: Error bounds for different target pattern order. The solid lines depict the results for the exact inversion in the N_c-subspace and the dashed lines depict the results for the approximate inversion considering higher order harmonics

Chapter III

RADIAL DIRECTIVITY CONTROL

3.1 Introduction

As described in the previous chapter, synthesis of order-limited radiation patterns is feasible with spherical loudspeaker arrays. In general finding optimal weights to map the base functions on the monophonic loudspeaker signals provides pattern-matching on a synthesis sphere S_a with a radius r_a. As shown for the IEM icosahedral loudspeaker array, proper weights can be found by acoustic measurements. In this case the desired pressure pattern is generated on a sphere determined by the measurement grid. Alternatively appropriate weights to synthesize particle velocity patterns on the array surface S_0 with radius r_0 can be derived, e.g. by an analytic model [ZH07] or measurements of the membrane velocity of the transducers with a laser Doppler vibrometer [RJ07, JR07]. Hence, we will distinguish two possible scenarios, depending on the design of the angular directivity control. Figure 14 sketches both basic arrangements. The red dotted circle indicates the synthesis sphere of the angular directivity control. Due to wave propagation, the a synthesized pattern appears blurred at other radii. To synthesize a desired sound pressure pattern on a sphere with arbitrary radius r_p, indicated by the blue dotted circle, it is necessary to compensate for the radial wave propagation.

Therefore a radial directivity control is introduced which is developed in the following. Considering the radial wave propagation, analytic descriptions for adequate equalization filters are derived. Based on the analytic descriptions it is shown how to efficiently implement these filters in discrete-time via bilinear transform (cf. Daniel [Dan03]) and newly impulse invariance variations.

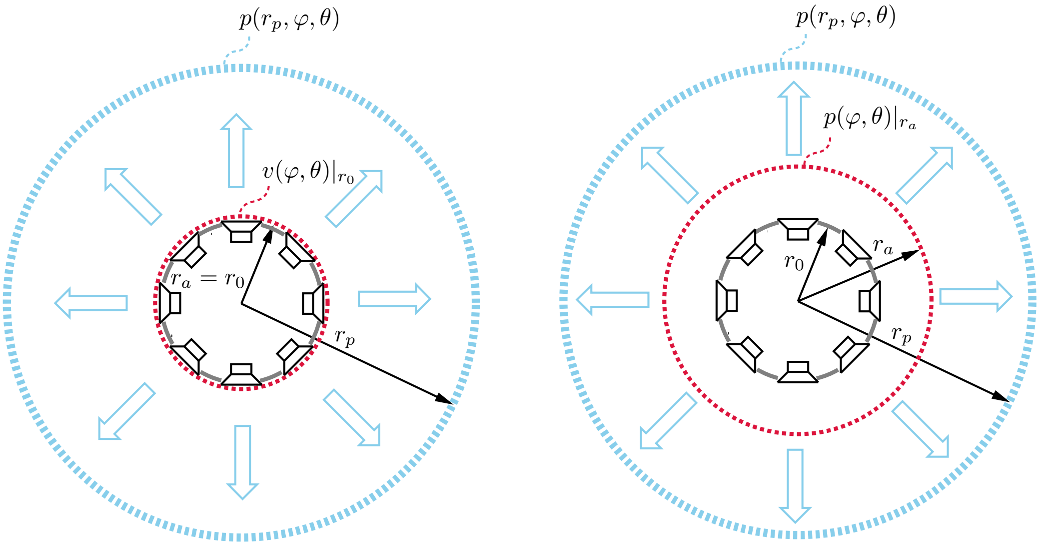

(a) **(b)**

Figure 14: Two basic arrangements for angular directivity pattern synthesis: a) synthesizing a particle velocity pattern on the array surface and b) synthesizing a pressure pattern on a fixed sphere with radius r_a. The red dotted circle indicates the synthesis sphere S_a of the angular directivity control. Introducing a radial directivity control, the synthesized pattern can be projected to a variable sphere S_p indicated by the dotted blue circle.

3.2 Extrapolation of the Spherical Wave Spectra

For a homogeneous fluid with no viscosity, the acoustic wave propagation is described by the homogeneous lossless wave equation:

$$\Delta p(r, \varphi, \theta, t) - \frac{1}{c^2}\frac{\partial^2 p(r, \varphi, \theta, t)}{\partial^2 t} = 0 \tag{3.1}$$

where p is the sound pressure at the spatial location (r, φ, θ) and time t, c is the speed of sound in the medium[1] and Δ is the the Laplace operator, which for a function f equals:

$$\Delta f = \frac{1}{r^2}\frac{\partial}{\partial r}\left(r^2 \frac{\partial f}{\partial r}\right) + \frac{1}{r^2 \sin\theta}\frac{\partial}{\partial \theta}\left(\sin\theta \frac{\partial f}{\partial \theta}\right) + \frac{1}{r^2 \sin\theta}\frac{\partial^2 f}{\partial^2 \varphi} \tag{3.2}$$

in the spherical coordinate system. The general solution for Eq.(3.1) is given by separation of variables, cf. [Wil99]:

$$p(r, \varphi, \theta, t) = R(r)\Phi(\varphi)\Theta(\theta)T(t) \tag{3.3}$$

This leads to an ordinary differential equation for each variable. It shows, that the solutions for the angular differential equations are given by exponential and Legendre functions and thus can be combined to spherical harmonic base functions $Y_n^m(\varphi, \theta)$,

---

[1] $c = 343 m/s$@20°C in air

whereas the spherical Hankel functions of the first and second kind $h_n^{(1,2)}$ are solutions to the radial differential equation. Regarding just harmonic processes $T(t) = e^{i\omega t}$ and an exterior problem, where all sources are located inside a boundary sphere, the solution in the frequency domain reads as:

$$p(r, \varphi, \theta) = \sum_{n=0}^{\infty} \sum_{m=-n}^{n} C_{mn}(\omega) h_n^{(2)}(kr) Y_n^m(\varphi, \theta) \tag{3.4}$$

where $k = \frac{\omega}{c}$ is the wavenumber and the terms C_{mn} are defined by the boundary values of the problem. In the following developments explicit notation of the frequency dependence is dropped for notational convenience. Moreover the index to distinguish between spherical Hankel functions of first and second kind is omitted and hereafter h_n denotes the second kind.

Knowing the coefficients C_{nm}, the sound pressure for every field point located outside the boundary sphere could be determined and that means the radiated pressure field is completely defined.

Applying Eq.(2.9) to Eq.(3.4) reveals the relation of C_{nm} to the spherical wave spectrum:

$$\psi_{nm}(r) = \int_{\Omega} p(r, \varphi, \theta) Y_n^{m*} d\Omega = C_{nm} h_n(kr) \tag{3.5}$$

Thus given the pressure spectrum located at r_a allows to detrimine C_{nm}:

$$C_{nm} = \frac{\psi_{nm}(r_a)}{h_n(kr_a)} \tag{3.6}$$

Plugging this into Eq.(3.5) yields the extrapolation relation for the sound pressure wave spectrum:

$$\psi_{nm}(r) = \frac{h_n(kr)}{h_n(kr_a)} \psi_{nm}(r_a) \tag{3.7}$$

Similarly a relation between velocity and pressure spectra can be found starting with Euler's equation:

$$i\rho_0 c \boldsymbol{v}(r, \varphi, \theta) = \boldsymbol{\nabla} p(r, \varphi, \theta) \tag{3.8}$$

where the $\boldsymbol{\nabla}$ operator in spherical coordinates yields:

$$\boldsymbol{\nabla} f = \frac{\partial f}{\partial r} \boldsymbol{e}_r + \frac{1}{r} \frac{\partial f}{\partial \theta} \boldsymbol{e}_\theta + \frac{1}{r \sin\theta} \frac{\partial f}{\partial \phi} \boldsymbol{e}_\phi \tag{3.9}$$

Applying Eq. (2.9) to the radial gradient from Eq. (3.8) leads to an representation of Euler's equation for the spherical wave spectra of the radial particle velocity:

$$i\rho_0 c \Upsilon_{nm}(r) = \frac{d\psi_{nm}(r)}{dr} \tag{3.10}$$

Inserting Eq.(3.5) leads to:

$$\Upsilon_{nm}(r) = \frac{h'_n(kr)}{i\rho_0 c} C_{nm} \tag{3.11}$$

and hence knowing the spherical wave spectrum of the particle velocity at a certain radius r_a, the coefficients $C_n m$ are obtained by:

$$C_{nm} = i\rho_0 c \frac{1}{h'_n(kr_a)} \Upsilon_n^m(r_a) \tag{3.12}$$

Plugging this into Eq.(3.5) yields the relationship velocity and pressure spectra:

$$\psi_{nm}(r) = i\rho_0 c \frac{h_n(kr)}{h'_n(kr_a)} \Upsilon_{nm}(r_a) \tag{3.13}$$

3.3 Radial Steering Filter

The fractions in Eqs.(3.13) and (3.7) can be interpreted as transmission terms for the spherical wave spectra. Thus to synthesize a pressure pattern on the target sphere S_p, the pattern synthesized on S_a needs an appropriate equalization. To achieve an adequate compensation, a set of radial steering filters (RSF) $H_n^{(eq)}$ is perpended to the angular directivity control, like depicted in Figure 15.

Consequently the frequency response of the RFS is required to be inverse to the according propagation terms. Depending on whether a velocity or a pressure pattern is synthesized, two different kinds of radial steering filters are suitable. The constant multipliers $1/\rho_0 c$ in the first equation is dropped for abbreviation:

$$H_n^{(eq,v)}(\omega) = i\frac{h'_n(kr_a)}{h_n\left(kr_p\right)} \tag{3.14}$$

$$H_n^{(eq,p)}(\omega) = \frac{h_n(kr_a)}{h_n\left(kr_p\right)} \tag{3.15}$$

It is easy to see, that the RSF are equal for all $2n + 1$ degrees of an order n and only depend on the radius of the primary sphere r_a and the radius of the sphere r_p, where the pattern shall be projected to.

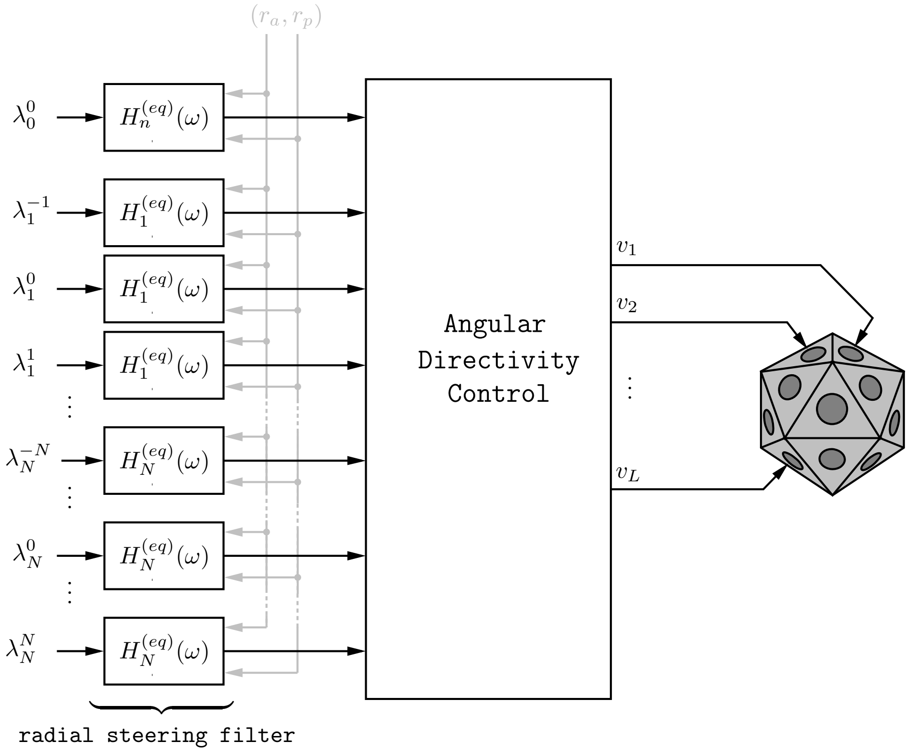

Figure 15: Control unit with a set of radial steering filters

Dynamic Range Requirements: Figure 16 and 17 show the magnitude responses of the two different types of radial steering filters subject to different target distances r_p and up to a spherical harmonic order of 3. It is seen that the required dynamic range for both types of radial steering filters increases with increasing target distances and spherical harmonic orders.

As an example, a spendable dynamic range of 40dB for filter implementation is assumed. In Figure 16 the lower cutoff frequencies due to this dynamic limitation are indicated by a red dots. Considering the upper frequency bound due to spatial aliasing of the spherical loudspeaker array, indicated by a vertical dashed line, a feasible synthesis frequency range results for the overall system. In the second scenario Figure 17, there is usually no information about the aliasing frequency, i.e. the array geometry.

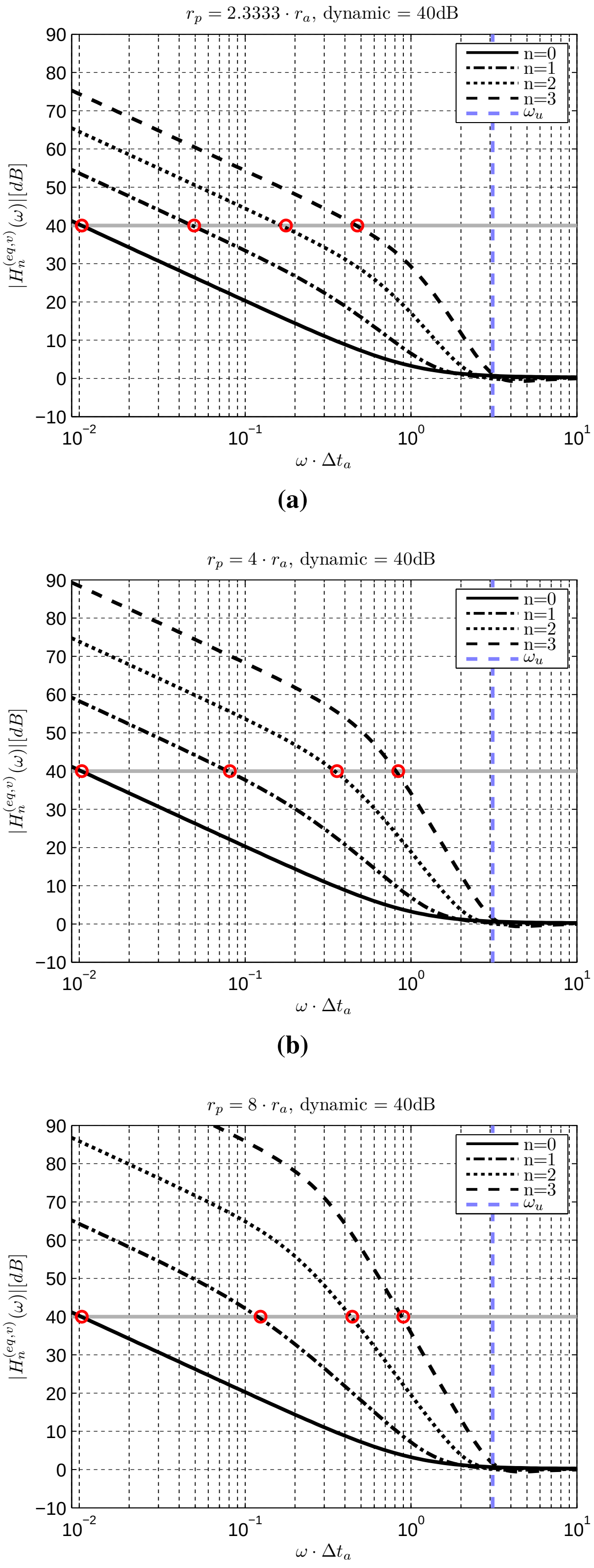

(a)

(b)

(c)

Figure 16: Magnitude response of $H_n^{(eq,v)}$ for a) $r_p = 2.333 \cdot r_a$ b) $r_p = 4 \cdot r_a$ c) $r_p = 8 \cdot r_a$. Given dynamic range of 40 dB, the red dots indicate the lower cutoff frequency for each spherical harmonic order. The dashed vertical line indicates the upper cutoff frequency due to spatial aliasing.

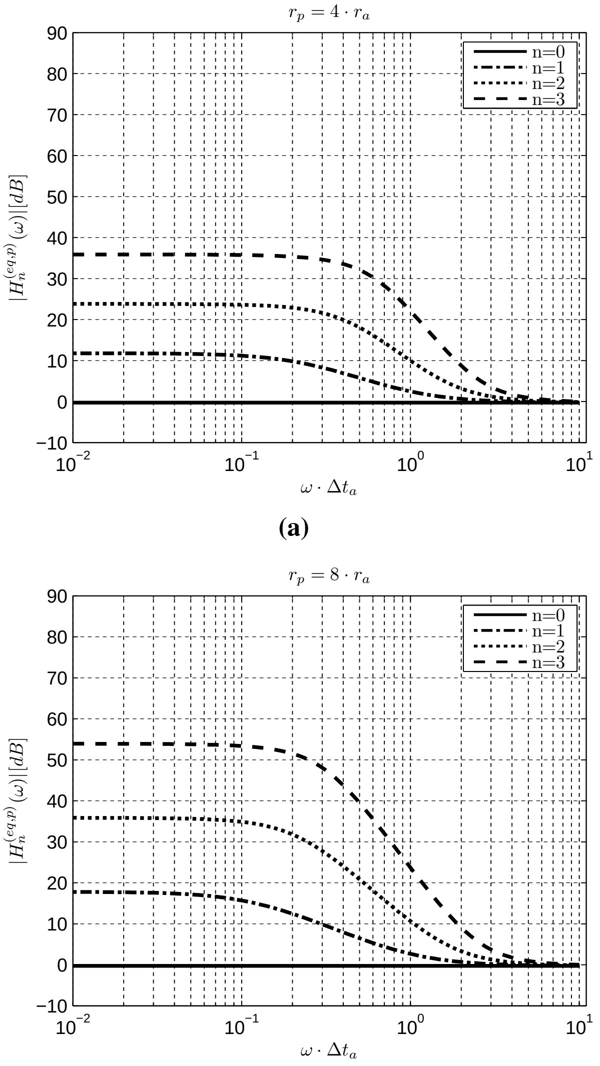

(a)

(b)

Figure 17: Magnitude response of $H_n^{(eq,p)}$ for a) $r_p = 4 \cdot r_a$ b) $r_p = 8 \cdot r_a$

3.4 Spherical Hankel Functions

In this section a compact Laplace domain representation for the spherical Hankel functions and their derivatives will be derived and a recurrence relation for the associated coefficients will be given.

Definition:

$$h_n(kr) = -i^n \frac{e^{-ikr}}{(ikr)^{n+1}} \sum_{l=0}^{n} \frac{(n+l)!}{l!(n-l)!2^l} (ikr)^{n-l} \tag{3.16}$$

$$h_n'(kr) = h_{n-1}(kr) - \frac{n+1}{kr} h_n(kr) \tag{3.17}$$

This definitions where taken from [GD05] and are slightly rearranged according to Zotter Noisternig [ZN07] to simplify the following derivations.

Laplace Domain: The Fourier transform is related to the Laplace transform by:

$$F(\omega) = \mathcal{F}\{f(t)\} = \mathcal{L}\{f(t)\}|_{s=j\omega} = F(s)|_{s=j\omega} \tag{3.18}$$

Recalling $kr = \omega\Delta t$, Eq.(3.16) is easily transformed into the Laplace-domain by replacing $i\omega$ by s:

$$h_n(s\Delta t) = -i^n \frac{e^{-s\Delta t}}{(s\Delta t)^{n+1}} \sum_{l=0}^{n} \frac{(n+l)!}{l!(n-l)!2^l}(s\Delta t)^{n-l} \tag{3.19}$$

Changing the summation index in the equation above yields:

$$h_n(s\Delta t) = -i^n \frac{e^{-s\Delta t}}{(s\Delta t)^{n+1}} \sum_{k=0}^{n} \frac{(2n-k)!}{(n-k)!k!2^{n-k}}(s\Delta t)^{k}\,, \tag{3.20}$$

Thus the equation can be written in an abbreviated way:

$$h_n(s\Delta t) = -i^n e^{-s\Delta t} \frac{\sum\limits_{k=0}^{n} \beta_n(k)\cdot(s\Delta t)^k}{(s\Delta t)^{n+1}} \tag{3.21}$$

and the coefficients $\beta_n(k)$ of the numerator polynomials can be determined by a recurrence relation:

$$\beta_n(n) = 1 \qquad\qquad \forall\, n \geq 0\,, \tag{3.22}$$

$$\beta_n(k) = \frac{(2n-k-1)(2n-k)}{2(n-k)} \cdot \beta_{n-1}(k) \tag{3.23}$$

For the derivative of the spherical Hankel functions similarly results:

$$h_n'(s\Delta t) = i^{n+1} e^{-s\Delta t} \frac{\sum\limits_{k=0}^{n+1} \beta_n'(k)\cdot(s\Delta t)^k}{(s\Delta t)^{n+2}}. \tag{3.24}$$

$$\beta_0'(k) = -\tilde{b}_1(k) \tag{3.25}$$

$$\beta_n'(k) = (n+1)\cdot\beta_n(k) + \beta_{n-1}(k-2) \tag{3.26}$$

Note that in the following the delays $e^{-s\Delta t}$ are omitted since they are not always compensable by causal filters.

3.5 Impulse Invariance Method

3.5.1 Preliminary Remarks - Corrected Application

A continuous-time impulse response[1] $g(t)$ is related to its impulse-invariant discrete-time counterpart $g[n]$ by (cf. Oppenheim [OSB99]):

$$g[n] = T \cdot g(nT) \tag{3.27}$$

where $T = \frac{1}{f_s}$ is the sampling period. This approach will be referred to as the impulse invariance method (IIM). Sampling the continuous-time impulse response, special attention should be paid to discontinuities in $g(t)$. In case of a jump discontinuity, the classical method (cf. [OSB99]) assigns the right-hand limit L^+ of the jump to the corresponding sample value. As a catchy example, assuming $g(t)$ is the unit-step function $u(t)$, having a discontinuity at $t = 0$, this leads to:

$$g[n] = Tu[n] \tag{3.28}$$

where the discrete-time unit-step function is defined by:

$$u[n] = \begin{cases} 1, & n \geq 0 \\ 0, & n < 0 \end{cases} \tag{3.29}$$

A correction to the IIM has been suggested by Mecklenbräucker [Mec00] and Jackson [Jac00]. Both independently has pointed out, that assigning the arithmetic mean of the left-hand and right-hand limit of a jump at $g[0]$ is a more accurate choice. Doing so, $\sum g[n]$ yields a better approximation of $\int g(t)dt$. This corrected version will be referred to as the corrected impulse invariance method (CIIM).

Keeping in mind that the continuous-time unit-step function $u(t)$ is not uniquely defined for $t = 0$, this correction is consistent with the conventional definition of $u(t)$ in the face of the Laplace transform (c.f. [AS65] p. 1020):

$$u(t) = \begin{cases} 1, & t > 0 \\ \frac{1}{2}, & t = 0 \\ 0, & t < 0 \end{cases} \tag{3.30}$$

---

[1] To avoid a confusion with the spherical Hankel functions, the impulse response is denoted by $g(t)$ and the transfer function by $G(s)$, following the common nomenclature in control engineering.

Thus for an accurate sampled counterpart of the unit-step function defined like above, Eq.(3.28) has to be rewritten as:

$$g[n] = T\left(u[n] - \frac{1}{2}\delta[n]\right) \tag{3.31}$$

Like shown in [Jac00, Mec00] the application of the corrected impulse invariance method (CIIM) yields a better discrete-time filter approximation, but the aliasing error due to under sampling is still present.

The classical approach and the corrected version as well can only handle strictly popper transfer fucntions, sc. the degree of the numerator is less than the degree denominator.

Eitelberg in [Eit06] re-interprets the impulse invariance method as a convolution invariance. This automatically leads to the corrected impulse invariance, and furthermore a method is suggested for transfer functions that are proper, but not strictly proper, sc. having a direct throughput or high frequency gain K_{hf}. The overall system can be split up into K_{hf} and a parallel low-pass part:

$$g(t) = g_{lp}(t) + K_{hf}\delta(t) \tag{3.32}$$

Since $g_{lp}(t)$ is strictly proper, its impulse invariant discrete-time counterpart $g_{lp}[n]$ exists and the overall system yields:

$$g[n] = g_{lp}[n] + K_{hf}\delta[n] \tag{3.33}$$

Although this is not relevant here, note that transfer functions containing multiple-order poles should be handled carefully since “the most prominent available works contain errors”, cf. [Cav96].

An equivalent treatment of the CIIM expressed with state variables has been suggested by Nelatury in [Nel07]. This approach is capable to cope with repeated poles and further a pre-warping procedure is proposed in this work, aiming at a reduction of aliasing errors.

3.5.2 Partial Fraction Expansion (PFE)

The straightforward approach for discrete-time representations of the radial steering filter is the direct application of the CIIM to the continuous-time expressions given in Eqs.(3.14) and (3.15). Insertion of the Laplace-transform of the spherical Hankel functions, cf. Eqs.(3.21) and (3.24), yields the RSF in the Laplace-domain:

$$H_n^{(eq,v)}(s) = \frac{\sum_{k=0}^{n+1} \beta_n'(k) \cdot s^k \Delta {t_a}^{k-n-2}}{\sum_{k=0}^{n} \beta_n(k) s^{k+1} \Delta {t_p}^{k-n-1}} \tag{3.34}$$

$$H_n^{(eq,p)}(s) = \frac{\sum_{k=0}^{n} \beta_n(k) s^k \Delta {t_a}^{k-n-1}}{\sum_{k=0}^{n} \beta_n(k) s^k \Delta {t_p}^{k-n-1}} \tag{3.35}$$

where Δt_a and Δt_p are the acoustic delays corresponding to r_a and r_p, cf. Eqs.(3.14) and (3.14).

Partial Fraction Expansion: Ususally the application of the impulse-invariance method is performed by expanding the transfer function into a sum of first-order partial fractions and transforming each term independently. Assuming the absence of multiple poles, the PFE for a rational function with numerator degree I and denominator degree J shows the following structure:

$$\frac{B(s)}{A(s)} = \sum_{j=1}^{J} \frac{r_j}{s - s_j} + d(s) \tag{3.36}$$

where r_j is the coefficient of pole s_j and $d(s)$ is the direct-term respectively a FIR-part of order K. Since $d(s)$ is the result of the polynomial long division of numerator and denominator polynomial,

$$K = I - J \qquad \text{if } I - J \geq 0 \tag{3.37}$$

$$d(s) = 0 \qquad \text{if } I - J < 0 \tag{3.38}$$

Hence expressing Eq.(3.34) and Eq.(3.35) in terms of partial fractions, the following structure emerges:

$$H_n^{(eq,v)}(s) = d + \frac{r_0}{s} + \frac{r_r}{s - s_r} \cdot \mathrm{mod}(n,2) + \sum_{l=1}^{\mathrm{div}(n,2)} \left(\frac{r_l}{s - s_l} + \frac{r_l^*}{s - s_l^*} \right) \tag{3.39}$$

$$H_n^{(eq,p)}(s) = d + \frac{r_r}{s - s_r} \cdot \mathrm{mod}(n,2) + \sum_{l=1}^{\mathrm{div}(n,2)} \left(\frac{r_l}{s - s_l} + \frac{r_l^*}{s - s_l^*} \right) \tag{3.40}$$

with s_r and s_l being the real and complex roots of the denominator polynomial.

Determining the roots of polynomials is a challenging topic, but straightforward applying a numerical root-finding algorithm[1]. Knowing s_r and s_l, the associated coefficients r_r and r_l can be determined by comparison of coefficients.

Note since $H_n^{(eq,v)}(s)$ and $H_n^{(eq,p)}(s)$ have the same numerator polynoial, s_r and s_l in Eqs.(3.39) and (3.40) are identical. Even though this is not true for the residues, an additional index to indicated this was omitted.

Application of the CIIM[2] to each summand in Eqs.(3.39) and (3.40) yields a discrete-time representation:

$$H_n^{(eq,v)}(z) = d + \frac{b_{0,0} + b_{1,0}z^{-1}}{1 - z^{-1}} + \frac{b_{0,r} + b_{1,r}z^{-1}}{1 + a_{1,r}z^{-1}} \cdot \mathrm{mod}(n,2) + \sum_{l=1}^{\mathrm{div}(n,2)} \frac{b_{0,l} + b_{1,l}z^{-1} + b_{2,l}z^{-2}}{1 + a_{1,l}z^{-1} + a_{2,l}z^{-2}} \tag{3.41}$$

$$H_n^{(eq,p)}(z) = d + \frac{b_{0,r} + b_{1,r}z^{-1}}{1 + a_{1,r}z^{-1}} \cdot \mathrm{mod}(n,2) + \sum_{l=1}^{\mathrm{div}(n,2)} \frac{b_{0,l} + b_{1,l}z^{-1} + b_{2,l}z^{-2}}{1 + a_{1,l}z^{-1} + a_{2,l}z^{-2}} \tag{3.42}$$

where the filter coefficients are obtained by the equations in Table 1. Due to the complex-conjugate symmetry, all the coefficients become real valued. As shown by the signal-flow graph in Figure 18, the implementation of Eqs.(3.41) and (3.42) yields a parallel structure. In case of variable radial distances, the filter coefficients obviously have to be recomputed whenever a distance value is changed. In common applications only the projection radius will change, whereas the aperture radius is fixed. A change of r_p leads to different numerator coefficients in Eqs.(3.34) and (3.35), implying that the PFE has to be applied repeatedly.

---

[1] For this work the MATLAB® function *roots* was used.

[2] A detailed derivation for a FOS respectively a pair of complex-conjugate FOS is given in appendix

Table 1: coefficients for the PFE implementation

$b_{0,0} = \frac{T}{2}\, r_0$,	$b_{1,0} = \frac{T}{2}\, r_0$	
$b_{0,r} = \frac{T}{2}\, r_r$,	$b_{1,r} = \frac{T}{2}\, r_r\, e^{s_r T}$,	$a_{1,r} = -e^{s_r T}$
$b_{0,l} = \frac{T}{2}\left(r_l + r_l^*\right)$,	$b_{1,l} = \frac{T}{2}\left(r_l - r_l^*\right)\left(e^{s_l T} - e^{s_l^* T}\right)$,	$b_{2,l} = -\frac{T}{2}(r_l + r_l^*)e^{\left(s_l+s_l^*\right)T}$
	$a_{1,l} = -\left(e^{s_l} + e^{s_l^*}\right)$,	$a_{2,l} = e^{\left(s_l+s_l^*\right)T}$

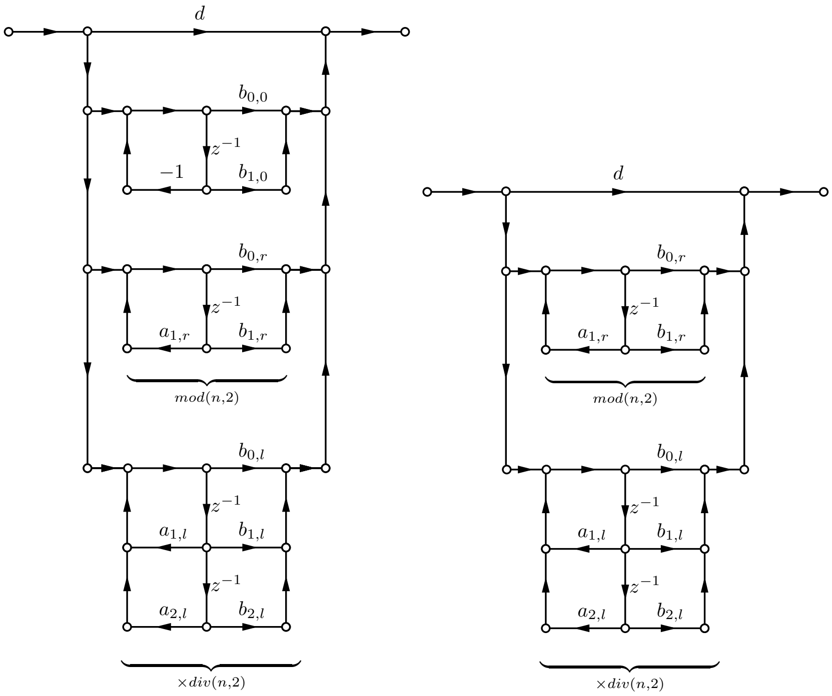

(a) **(b)**

Figure 18: Signal-flow graph of (a)$H_n^{(eq,v)}$ and (b)$H_n^{(eq,p)}$ in parallel structure (DF-II).

3.5.3 Factorized Second Order Sections

To simplify the following derivations, a substitution of $\tilde{s} = s\Delta t$ is introduced in Eq.(3.21) and (3.24):

$$h_n(\tilde{s}) = -i^n \frac{\sum_{k=0}^{n} \beta_n(k) \cdot \tilde{s}^k}{\tilde{s}^{n+1}} \tag{3.43}$$

$$h'_n(\tilde{s}) = i^{n+1} \frac{\sum_{k=0}^{n+1} \beta'_n(k) \cdot \tilde{s}^k}{\tilde{s}^{n+2}} \tag{3.44}$$

The substitution can also be interpreted as a normalization of h_n and h'_n, since the dependence on Δt respectively r is pushed into $\tilde{s}$.

From the fundamental theorem of algebra we know that every complex polynomial has exactly as many complex roots as its degree and furthermore, for real valued coefficients also the roots are real or come in complex pairs. This implies, that polynomials with only real and complex-conjugate zeros would expand to real-valued coefficients only. For a second-order polynomial with complex-conjugate zeros[1] this means:

$$(s - s_i)(s - s_i^*) = (s - \alpha_i)^2 + \omega_i^2 \ , \tag{3.45}$$

where $\alpha_i = \mathrm{Re}(s_i)$ and $\omega_i = \mathrm{Im}(s_i)$.

Hence restricting all the coefficients to be real, we can factorize the numerator polynomials from Eq.(3.43) and (3.44) into a product of second order sections (SOS), representing the complex-conjugate root pairs and first order sections (FOS) representing the real roots.

The real and imaginary parts of the complex-conjugate numerator roots of in Eq.(3.43) are denoted by $\tilde{\alpha}_l$ and $\tilde{\omega}_l$ and analogously $\tilde{\alpha}'_l$ and $\tilde{\omega}'_l$ are the roots in Eq.(3.44). For a consistent notation the real roots are named $\tilde{\alpha}_r$ respectively $\tilde{\alpha}'_r$ and the tilde symbol refers to the normalization.

A.1, cf. Eqs.(A.4) and (A.5).

[1] Referring to the physical meaning of such an polynomial as transfer function denominator, α is also known as damping constant and ω as angular frequency of a an exponential decaying oscillation.

Consequently, a factorized version of Eqs.(3.43) and (3.44) is expressed by:

$$h_n(\tilde{s}) = -i^n \frac{1}{\tilde{s}} \left(\frac{\tilde{s} - \tilde{\alpha}_r}{\tilde{s}} \right)^{\mathrm{mod}(n,2)} \cdot \prod_{l=1}^{\mathrm{div}(n,2)} \frac{(\tilde{s} - \tilde{\alpha}_l)^2 + \tilde{\omega}_l^2}{\tilde{s}^2} \tag{3.46}$$

$$h_n'(\tilde{s}) = i^{n+1} \frac{1}{\tilde{s}} \left(\frac{\tilde{s} - \tilde{\alpha}_r'}{\tilde{s}} \right)^{\mathrm{mod}(n+1,2)} \cdot \prod_{l=1}^{\mathrm{div}(n+1,2)} \frac{\left(\tilde{s}^2 - \tilde{\alpha}_l'\right)^2 + \tilde{\omega}_l'^2}{\tilde{s}^2} \tag{3.47}$$

From this normalized functions, the factorized expression for a specific delay time is obtain by back substitution $\tilde{s} = s\Delta t$:

$$h_n(s\Delta t) = -i^n \frac{1}{s\Delta t} \left(\frac{s - \alpha_r}{s} \right)^{\mathrm{mod}(n,2)} \cdot \prod_{l=1}^{\mathrm{div}(n,2)} \frac{(s - \alpha_l)^2 + \omega_l^2}{s^2} \tag{3.48}$$

$$h_n'(s\Delta t) = i^{n+1} \frac{1}{s\Delta t} \left(\frac{s - \alpha_r'}{s} \right)^{\mathrm{mod}(n+1,2)} \cdot \prod_{l=1}^{\mathrm{div}(n+1,2)} \frac{\left(s^2 - \alpha_l'\right)^2 + \omega_l'^{\,2}}{s^2}, \tag{3.49}$$

Comparing Eq.(3.48) and Eq.(3.49) with Eqs.(3.48) and (3.49), it becomes evident, that $\alpha = \frac{\tilde{\alpha}}{\Delta t}$ and $\omega = \frac{\tilde{\omega}}{\Delta t}$. Thus the roots of the spherical Hankel functions for a specific radial distance r can be obtained by scaling the generalized roots via dividing by the delay time Δt.

Assembling the radial steering filters in Eqs.(3.14) and (3.15) by substiution of Eqs(3.48) and (3.49) yields:

$$H_n^{(eq,v)}(s) = \frac{1}{s} \cdot \frac{\left(s - \alpha_r'^{(a)}\right)^{\mathrm{mod}(n+1,2)}}{\left(s - \alpha_r^{(p)}\right)^{\mathrm{mod}(n,2)}} \cdot \frac{\prod_{l=1}^{\mathrm{div}(n+1,2)} \left(s - \alpha_l'^{(a)}\right)^2 + \omega_l'^{(a)\,2}}{\prod_{l=1}^{\mathrm{div}(n,2)} \left(s - \alpha_l^{(p)}\right)^2 + \omega_l^{(p)\,2}} \tag{3.50}$$

$$H_n^{(eq,p)}(s) = \left(\frac{s - \alpha_r^{(a)}}{s - \alpha_r^{(p)}} \right)^{\mathrm{mod}(n,2)} \cdot \prod_{l=1}^{\mathrm{div}(n,2)} \frac{\left(s - \alpha_l^{(a)}\right)^2 + \omega_l^{(a)\,2}}{\left(s - \alpha_l^{(p)}\right)^2 + \omega_l^{(p)\,2}} \tag{3.51}$$

The coefficient superscripts denote the scaling by the delays according to the projection radius respectively or the aperture radius, viz. $\alpha^{(a)} = \frac{\tilde{\alpha}}{\Delta t_a}$, $\alpha^{(p)} = \frac{\tilde{\alpha}}{\Delta t_p}$ (similarly for ω). The constant multipliers $\frac{\Delta t_p}{\Delta t_a}$ are omitted, since they are equal for all orders n and only represent the $\frac{1}{r}$ dependency of the sound pressure for spherical waves.

Whereas in Eq.(3.51) the multiplicative FOS and SOS terms are easy to see, for Eq.(3.50) the following rearrangement reveals its structure:

$$H_n^{(eq,v)}(s) = \left(\frac{s - \alpha_r'^{(a)}}{s} \right)^{\mathrm{mod}(n+1,2)} \cdot \left(\frac{\left(s - \alpha_L'^{(a)}\right)^2 + \omega_L'^{(a)\,2}}{s\left(s - \alpha_r^{(p)}\right)} \right)^{\mathrm{mod}(n,2)} \cdot \prod_{l=1}^{\mathrm{div}(n,2)} \frac{\left(s - \alpha_l'^{(a)}\right)^2 + \omega_l'^{(a)\,2}}{\left(s - \alpha_l^{(p)}\right)^2 + \omega_l^{(p)\,2}}$$

$$\text{where } L = \mathrm{div}(n+1, 2) \tag{3.52}$$

Applying the CIIM to each FOS/SOS independently leads to discrete-time filter representations showing the following structure:

$$H_n^{(eq,v)}(z) = \left(\frac{b_{0,r} + b_{1,r}\,z^{-1}}{1 - a_{1,r}\,z^{-1}}\right)^{\mathrm{mod}(n+1,2)} \cdot \left(\frac{b_{0,L} + b_{1,L}\,z^{-1} + b_{2,L}\,z^{-2}}{1 + a_{1,L}\,z^{-1} + a_{2,L}\,z^{-2}}\right)^{\mathrm{mod}(n,2)} \cdot \prod_{l=1}^{\mathrm{div}(n,2)} \frac{b_{0,l} + b_{1,l}\,z^{-1} + b_{2,l}\,z^{-2}}{1 + a_{1,l}\,z^{-1} + a_{2,l}\,z^{-2}} \tag{3.53}$$

$$H_n^{(eq,p)}(z) = \left(\frac{b_{0,r} + b_{1,r}\,z^{-1}}{1 + a_{1,r}\,z^{-1}}\right)^{\mathrm{mod}(n,2)} \cdot \prod_{l=1}^{\mathrm{div}(n,2)} \frac{b_{0,l} + b_{1,l}\,z^{-1} + b_{2,l}^{(a)}\,z^{-2}}{1 + a_{1l}\,z^{-1} + a_{2,l}\,z^{-2}} \tag{3.54}$$

The signal-flow graph of the implementation of Eq.(3.53) and (3.54) is shown in Figure 19. It is seen, that contrary to the parallel structure obtain by the PFE-approach, now results a cascade of FOS an SOS.

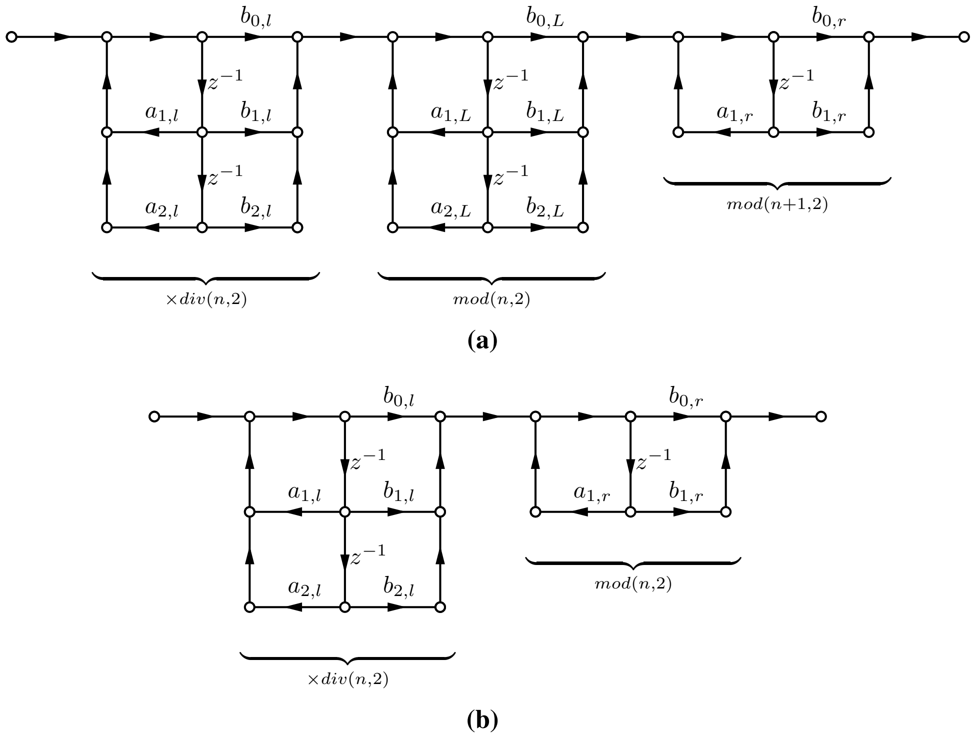

(a)

(b)

Figure 19: Signal-flow graph of (a)$H_n^{(eq,v)}$ and (b)$H_n^{(eq,p)}$ in cascade form (DF-II).

The CIIM transformations for each class of section is derived in Appendix A.1. Expressing the coefficients of Eq.(3.53) in terms of the general roots and replacing the continuous delay time by its discrete-time counterpart $\Delta n = \frac{\Delta t}{T}$, yields a set of simple equations for the filter coefficients. Analogously equations to calculate the coefficients

Table 2: Coefficients according to Eqs.(3.53) and (3.54)

$$
\begin{aligned}
b_{0,r} &= 1 - \frac{\tilde{\alpha}'_r}{2\Delta n_a} + \frac{\tilde{\alpha}_r}{2\Delta n_p}\,, \quad & b_{1,r} &= \left(\frac{\tilde{\alpha}_r}{2\Delta n_p} - \frac{\tilde{\alpha}'_r}{2\Delta n_a} - 1\right) e^{\frac{\tilde{\alpha}_r}{\Delta n_p}} \\
a_{1,r} &= -e^{\frac{\tilde{\alpha}_r}{\Delta n_p}}
\end{aligned}
$$

$$
\begin{aligned}
b_{0,L} &= \frac{\tilde{\alpha}_r}{2\Delta n_p} - \frac{\tilde{\alpha}'_L}{\Delta n_a} + 1\,, \quad & b_{2,L} &= \left(\frac{\tilde{\alpha}'_L}{\Delta n_a} - \frac{\tilde{\alpha}_r}{2\Delta n_p} + 1\right) e^{\frac{\tilde{\alpha}_r}{\Delta n_p}} \\
b_{1,L} &= \left(\frac{\tilde{\alpha}_r}{2\Delta n_p} - \frac{\tilde{\alpha}'_L}{\Delta n_a} + \frac{\tilde{\alpha}'^2_L + \tilde{\omega}'^2_L}{\tilde{\alpha}_r} \cdot \frac{\Delta n_p}{\Delta n_a^2}\right)\left(e^{\frac{\tilde{\alpha}_r}{\Delta n_p}} - 1\right) - e^{\frac{\tilde{\alpha}_r}{\Delta n_p}} - 1 \\
a_{1,L} &= -e^{\frac{\tilde{\alpha}_r}{\Delta n_p}} - 1\,, & a_{2,L} &= e^{\frac{\tilde{\alpha}_r}{\Delta n_p}}
\end{aligned}
$$

$$
\begin{aligned}
b_{0,l} &= \frac{\tilde{\alpha}_l}{\Delta n_p} - \frac{\tilde{\alpha}'_l}{\Delta n_a} + 1\,, \quad & b_{2,l} &= \left(\frac{\tilde{\alpha}'_l}{\Delta n_a} - \frac{\tilde{\alpha}_l}{\Delta n_p} + 1\right) e^{2\frac{\tilde{\alpha}_l}{\Delta n_p}} \\
b_{1,l} &= \left(\frac{\left(\frac{\tilde{\alpha}_l}{\Delta n_p} - \frac{\alpha'_l}{\Delta n_a}\right)^2 - \frac{\tilde{\omega}_l^2}{\Delta n_p^2} + \frac{\tilde{\omega}'^2_l}{\Delta n_a^2}}{\frac{\tilde{\omega}_l}{\Delta n_p}} \sin\left(\frac{\tilde{\omega}_l}{\Delta n_p}\right) - 2\cos\left(\frac{\tilde{\omega}_l}{\Delta n_p}\right)\right) e^{\frac{\tilde{\alpha}_l}{\Delta n_p}} \\
a_{1,l} &= -2\cos\left(\frac{\tilde{\omega}_l}{\Delta n_p}\right) e^{\frac{\tilde{\alpha}_l}{\Delta n_p}}\,, & a_{2,l} &= e^{2\frac{\tilde{\alpha}_l}{\Delta n_p}}
\end{aligned}
$$

in Eq.(3.54) can be developed. Both equation sets show a great similarity, thus in Table 2 the equations for Eq.(3.53) are given, with a few extensions[1] so that they are also valid for the coefficients in Eq.(3.54), after substituting the dashed quantities by the appropriate counterparts of the undifferentiated spherical Hankel function.

Having a closer look on Table 2, it can be seen, that the filter coefficients only depend on the general roots ($\tilde{\alpha}$, $\tilde{\omega}$), the aperture-radius of the loudspeaker array (Δn_a) and the projection radius (Δn_p). Thus the normalized roots can be determined once by a root-finding algorithm, stored in a look-up table and scaled by an arbitrary Δt. Hence in case of variable radial distances (viz. varying Δn_p) this provides an easy recomputation of the filter coefficients.

3.6 Bilinear Transform

Even though the focus of this work lies more on the impulse invariant method, in the following the applicability of the bilinear transform for the radial steering filter will be reviewed.

Referring to [OSB99], the bilinear transform corresponds to the substitution:

$$s = \frac{2}{T}\left(\frac{1 - z^{-1}}{1 + z^{-1}}\right) \tag{3.55}$$

This yields a mapping of the entire imaginary axis in the Laplace-domain onto one revolution of the unit circle in the z-domain, whereas the left half plane is mapped to the interior and the right half-plane to the exterior of the unit circle. Doing so, stability and minimum-phase properties are preserved and also aliasing is avoided since an infinitely high frequency will be mapped to the Nyquist frequency. But due to the non-linear mapping, a warping of the discrete-time frequency axis results. Thus at critically low sampling rates an unacceptable frequency warping may occur, what is the main drawback of this filter-design method.

The bilinear transform(BLT) can be expressed as a matrix multiplication followed by coefficient re-normalization (cf. [Chr03]). Given the coefficients of second-order

---

[1] Since α_r is always equal to zero in the FOS of $H_n^{(eq,v)}$, some terms vanish for the coefficients $b_{0,r}$, $b_{1,r}$ and $a_{1,r}$.

system in the Laplace-domain, and defining its bilinear transformed counterpart as,

$$G(s) = \frac{n_0\, s^2 + n_1\, s + n_2}{d_0\, s^2 + d_1\, s + d_2} \quad \xrightarrow{BLT} \quad G(z) = \frac{b_0 + b_1\, z^{-1} + b_2\, z^{-2}}{1 + a_1\, z^{-1} + a_2\, z^{-2}} \tag{3.56}$$

for a sampling frequency f_s, the discrete-time coefficients are obtained by the following matrix-equations:

$$\begin{bmatrix} \tilde{b}_0 & \tilde{b}_1 & \tilde{b}_2 \\ \tilde{a}_0 & \tilde{a}_1 & \tilde{a}_2 \end{bmatrix} = \begin{bmatrix} n_0 & n_1 & n_2 \\ d_0 & d_1 & d_2 \end{bmatrix} \cdot \begin{bmatrix} 4f_s^2 & -8f_s^2 & 4f_s^2 \\ 2f_s & 0 & -2f_s \\ 1 & 2 & 1 \end{bmatrix} \tag{3.57}$$

$$\begin{bmatrix} b_0 & b_1 & b_2 \\ 1 & a_1 & a_2 \end{bmatrix} = \frac{1}{\tilde{a}_0} \cdot \begin{bmatrix} \tilde{b}_0 & \tilde{b}_1 & \tilde{b}_2 \\ \tilde{a}_0 & \tilde{a}_1 & \tilde{a}_2 \end{bmatrix} \tag{3.58}$$

Similarly, a first-order system is transformed by a multiplication with a 2 × 2 matrix. This matrix is obtained from the 3 × 3 matrix in Eq.(3.57) by canceling the first line and the second row. Based on this, the transformation of a transfer function, split up in FOS and SOS, could be efficiently implemented. Since here the Laplace-variable is just substituted by an expression in z, for a higher order system it is irrelevant, apart from numerical issues, whether it is split up in parallel or cascaded SOS before the transformation is applied.

In the previous section it was shown, that the expression for the radial steering filter in factorized SOS form, given in Eqs.(3.51) and (3.52), is easy to adjust for variable radial distances. In combination with Eqs.(3.57) and (3.58), this yields a simple two-step algorithm to determine the filter coefficients:

1. Calculation of the Laplace-domain coefficients by scaling the generalized roots.
2. Performing the bilinear transform for each SOS respectively FOS.

3.7 Filter Design Evaluation

To evaluate the filter designs discussed, the deviation of the discrete-time transfer functions from their analytic analogons is considered on concrete examples.

3.7.1 Example 1: The IEM Icosahedral Loudspeaker Array

Recall the angular directivity control for the icosahedron, developed in Chapter 2, synthesizes a sound pressure distribution on the surface of the measurement grid, i.e. $r_p = 0.7m$. Furthermore we assume a target sphere with radius $r_p = 1.2m$ where the pattern shall be projected to and a sampling frequency of $f_s = 5512.5\,Hz$. Figure 20 shows the frequency responses of the appropriate discrete-time RSF $H_n^{(eq,p)}(z)$ up to a maximum order $N = 3$. The RSF obtained by the CIIM applied to the factorized SOS. The transfer function of the approximated filter does not deviated significantly from its analytic counterpart. Since the PFE approach and the bilinear transform show comparable good results, the corresponding diagrams are omitted.

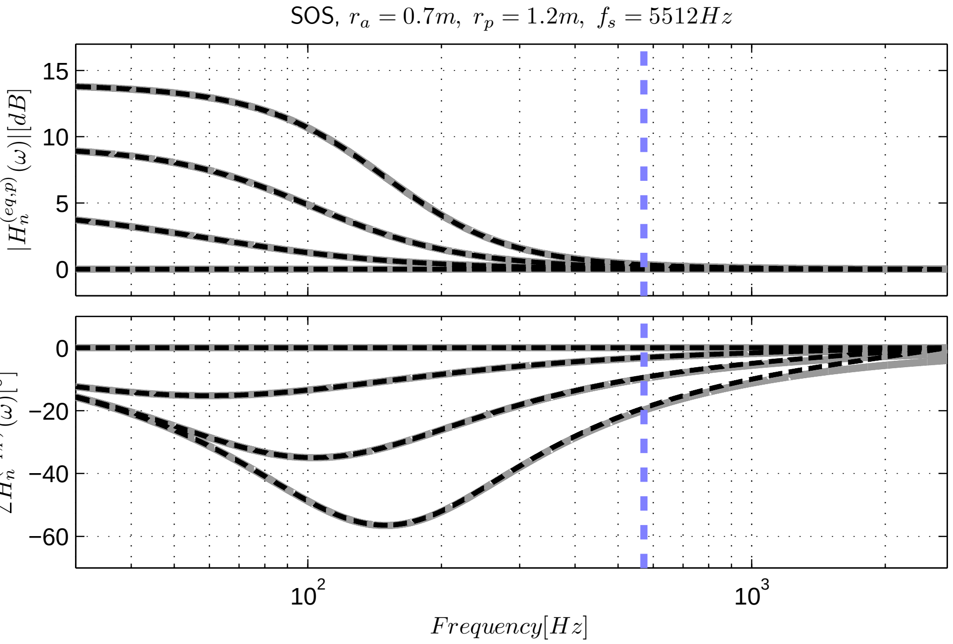

Figure 20: Frequency response of $H_n^{(eq,p)}(z)$ obtained by the CIIM applied to the factorized SOS. The solid gray line depicts the analytic function, the dashed black line the discrete-time approximation and the dashed vertical line indicates the upper cutoff frequency due to spatial aliasing.

3.7.2 Example 2: High Frequency Array

Since the errors of both transforms, in particular aliasing for the IIM and frequency warping for the bilinear transform, are more present at high frequencies, we consider an illustrative scenario for the errors. Thus a tweeter system for high frequency directivity synthesis with a small radius of $r_a = 0.075m$ is assumed, and a desired target radius $r_p = 1m$ for its radial steering filter of type $H_n^{(eq,v)}(z)$ at $f_s = 5512.5\,Hz$ selected. Figure 21, 22 and 23 show the match of the frequency responses for the different filter implementations. Comparing Figure 21, 22 and 23 it is seen, that the deviation of the discrete-time approximations in magnitude and phase differ, but seem to lie roughly in the same range. Thus a more detailed examination of the error is necessary to reveal the quality of the different methods. The frequency response error is introduced, representing the ratio of the discrete-time approximation and the analytic expression:

$$Error(\omega) = \frac{H(z)}{H(\omega)} \tag{3.59}$$

The frequency response error of $H_3^{(eq,v)}(z)$ is depicted in Figure 24. In this example, the CIIM applied to the factorized SOS outperforms the CIIM applied to PFE, whereas the phase error behaves contrarily. The bilinear transform shows the worst performance concerning the magnitude and phase matching in the feasible frequency range (beneath the upper cutoff frequency).

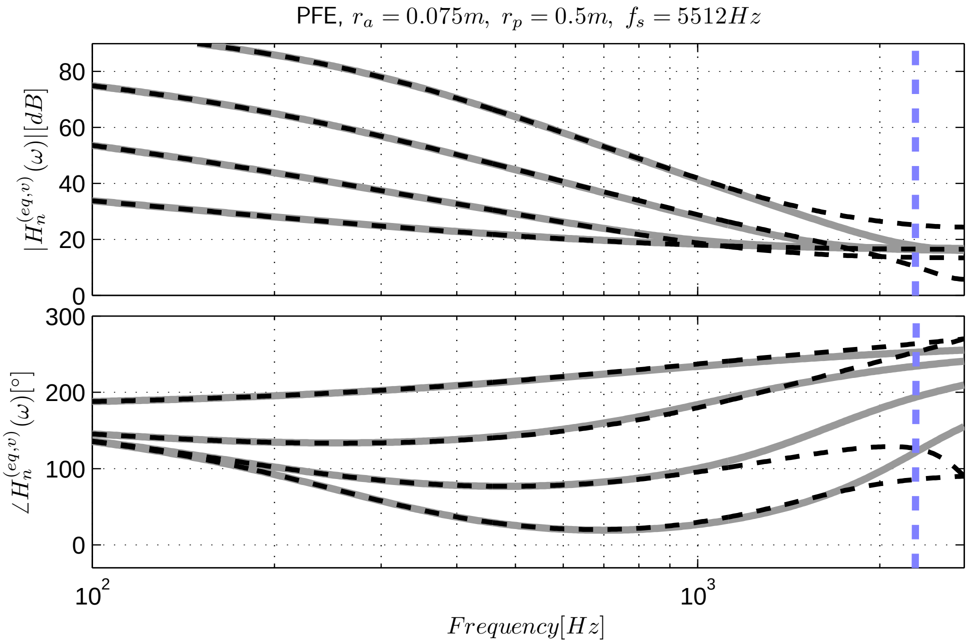

Figure 21: Frequency response of $H_n^{(eq,v)}(z)$, obtained by the CIIM applied to the PFE. The solid gray line depicts the analytic function, the dashed black line the discrete-time approximation and the dashed vertical line indicates the upper cutoff frequency due to spatial aliasing.

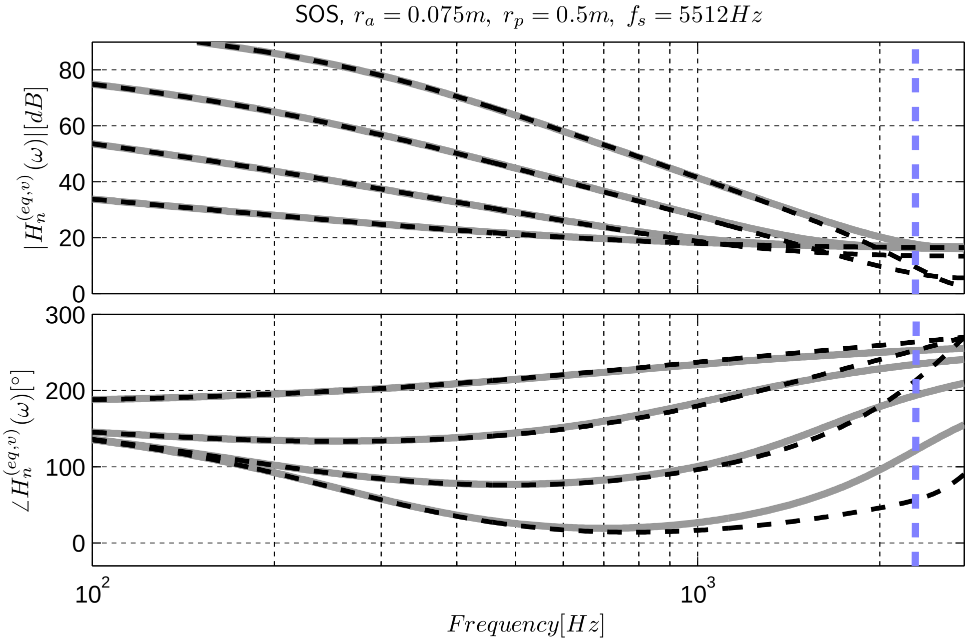

Figure 22: Frequency response of $H_n^{(eq,v)}(z)$ obtained by the CIIM applied to the factorized SOS. The solid gray line depicts the analytic function, the dashed black line the discrete-time approximation and the dashed vertical line indicates the upper cutoff frequency due to spatial aliasing.

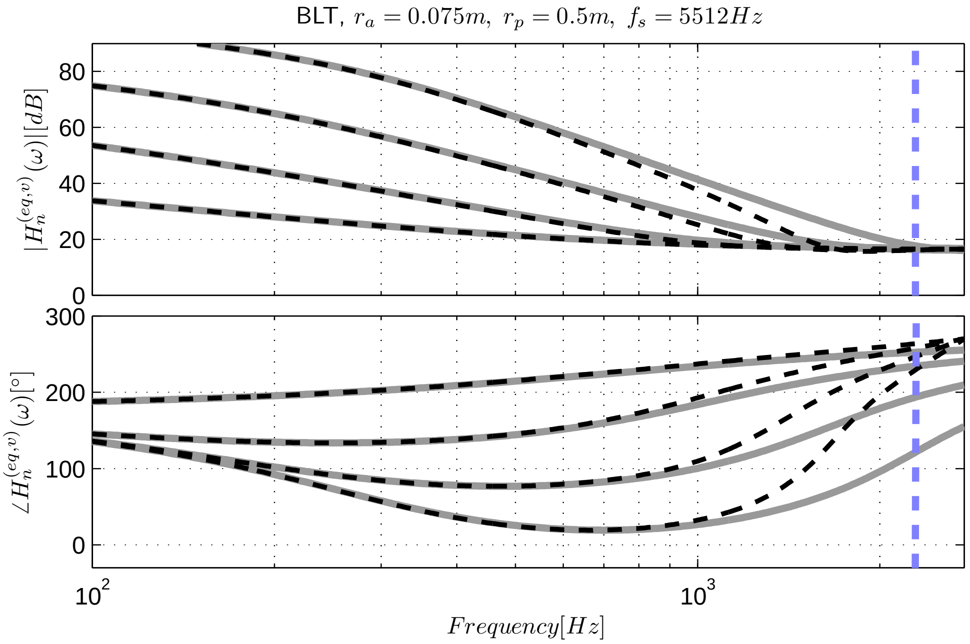

Figure 23: Frequency response of $H_n^{(eq,p)}(z)$, obtained by the bilinear transform. The solid gray line depicts the analytic function, the dashed black line the discrete-time approximation and the dashed vertical line indicates the upper cutoff frequency due to spatial aliasing.

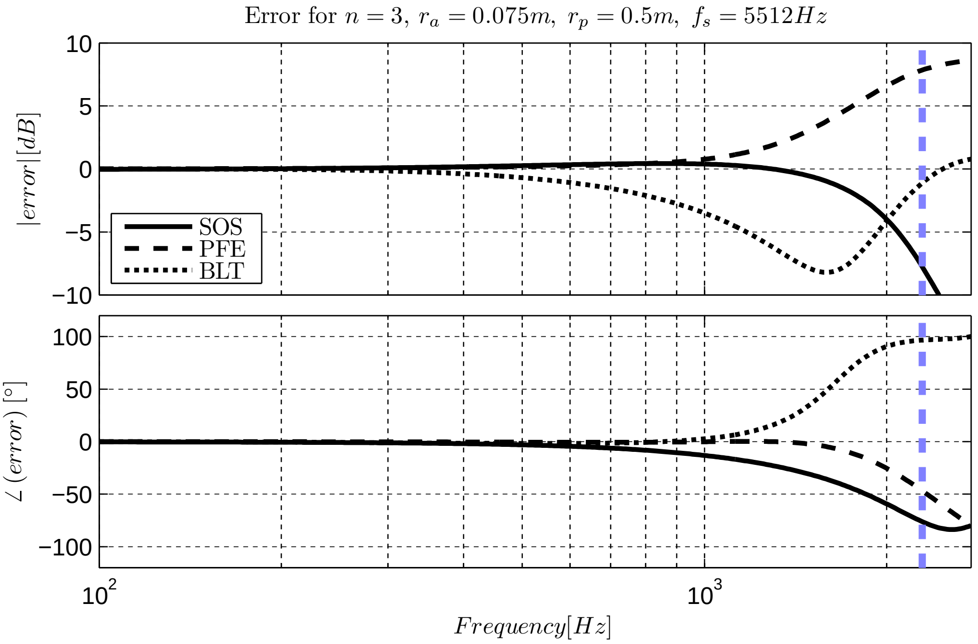

Figure 24: Error of the discrete-time approximations of $H_3^{(eq,v)}(\omega)$ by different filter implementations. The dashed vertical line indicates the upper cutoff frequency due to spatial aliasing.

Chapter IV

CONCLUSION

4.1 Angular Directivity Control

Chapter 2 has revealed a couple of interesting aspects considering angular directivity control based on measurements.

Applying the pseudo inverse to an equal angular resolution grid, a stable spherical harmonics decomposition is feasible up to high analysis orders. Additionally, adequate weighting of the sample values improves the accuracy of the pseudo inverse. Analysis up to order N requires $2\,(N+1)^2$ spatial samples. Exploiting the regular grid structure, in practice the $2\,(N+1)^2$ samples can be efficiently taken with a turntable and $N+1$ semicircularly arranged microphones.

Angular directivity control for spherical loudspeaker arrays is achieved by system inversion in the spherical harmonics domain. The application of a decoder reduces the dimension of the control system to the degrees of freedom of the array. This reduces the size of the control unit and thus the computational cost. System inversion can be done either exact in the array achievable subspace, or higher order harmonics can be considered. The latter yields an approximate inversion and suppresses spatial aliasing.

Instead of the considered all-or-none approaches for system inversion, perhaps a mix between aliasing suppression and the exact subspace control solution may show a favorable behavior and will be subject to future research.

4.2 Radial Directivity Control

Chapter 3 presented equalization filters compensating for the radial wave propagation. The analytic expressions, based on spherical Hankel functions, are realized with discrete-time IIR filters.

Impulse-invariant filter design yields very exact approximations if a recently introduced correction to the classical method is used. The corrected impulse-invariance method was applied to the analytic expressions in factorized second order sections or partial fractions. Comparable good results are achieved by the bilinear transform unless for adverse conditions, viz. low sampling rates alongside with small array diameters. In this case the CIIM applied to factorized SOS seems to yield the best magnitude approximation. Additionally, the filter coefficients of this structure are easy to adjust to variable radial distances.

Moreover, it should be noted that radial steering filters are also practicable to further applications, e.g. microphone arrays in open and closed sphere configurations.

Appendix A

DERIVATIONS

A.1 Impulse Invariance Method

A.1.1 Partial Fraction Expansion

Single Pole

$$\begin{aligned}
G(s) &= \frac{1}{s} \\
&\updownarrow \mathcal{L}^{-1} \\
g(t) &= u(t) \\
g[n] &= T\,u[n] - \frac{T}{2}\delta[n] \\
&\updownarrow \mathcal{Z} \\
G(z) &= \frac{T}{1-z^{-1}} - \frac{T}{2} \\
&= \frac{T}{2}\cdot\frac{1+z^{-1}}{1-z^{-1}}
\end{aligned} \tag{A.1}$$

$$\begin{aligned}
G(s) &= \frac{1}{s-a} \\
&\updownarrow \mathcal{L}^{-1} \\
g(t) &= e^{at}\cdot u(t) \\
g[n] &= T\,e^{anT}\,u[n] - \frac{T}{2}\delta[n] \\
&\updownarrow \mathcal{Z} \\
G(z) &= \frac{T}{1-e^{aT}\,z^{-1}} - \frac{T}{2} \\
&= \frac{T}{2}\cdot\frac{1+e^{aT}\,z^{-1}}{1-e^{aT}\,z^{-1}}
\end{aligned} \tag{A.2}$$

First Order Section

$$\begin{aligned}
G_{fos}(s) &= \frac{s-b_r}{s} = 1 - \frac{b_r}{s} \\
&\updownarrow \mathcal{L}^{-1} \\
g_{fos}(t) &= \delta(t) - b_r\,u(t) \\
g_{fos}[n] &= \delta[n] - T\,b_r\left(u[n] - \frac{1}{2}\delta[n]\right) \\
g_{fos}[n] &= \left(1 + \frac{1}{2}Tb_r\right)\delta[n] - T\,b_r u[n]
\end{aligned}$$

$$\updownarrow \mathcal{Z}$$

$$\begin{aligned}
G_{fos}(z) &= 1 + \frac{T}{2} b_r - \frac{T\,b_r}{1 - z^{-1}} \\
&= \frac{\left(1 + \frac{T}{2} b_r\right)\left(1 - z^{-1}\right) - T\,b_r}{1 - z^{-1}} \\
&= \frac{1 + \frac{T}{2} b_r - z^{-1} - \frac{T}{2} b_r z^{-1} - T\,b_r}{1 - z^{-1}} \\
&= \frac{1 - \frac{T}{2} b_r - \left(1 + \frac{T}{2} b_r\right) z^{-1}}{1 - z^{-1}}
\end{aligned} \tag{A.3}$$

Conjugate Complex Partial Fractions

$$\begin{aligned}
G_{sos}(s) &= \frac{r}{s - b} + \frac{r^*}{s - b^*} \\
&\updownarrow \mathcal{L}^{-1} \\
g_{sos}(t) &= r \cdot e^{bt} u(t) + r^* \cdot e^{b^* t} u(t) \\
g_{sos}[n] &= T\left(r \cdot \left(e^{bnT} u[n] - \frac{1}{2}\delta[n]\right) + r^* \cdot \left(e^{b^* nT} u[n] - \frac{1}{2}\delta[n]\right)\right) \\
&= T\left(r \cdot e^{bnT} u[n] + r^* \cdot e^{b^* nT} u[n] - \frac{r + r^*}{2}\delta[n]\right) \\
&\updownarrow \mathcal{Z} \\
G_{sos}(z) &= T\left(\frac{r}{1 - e^{bT} z^{-1}} + \frac{r^*}{1 - e^{b^* T} z^{-1}} - \frac{r + r^*}{2}\right) \\
&= \frac{T}{2} \cdot \frac{2r\left(1 - e^{b^* T} z^{-1}\right) + 2r^*\left(1 - e^{bT} z^{-1}\right) - (r + r^*)\left(1 - e^{bT} z^{-1}\right)\left(1 - e^{b^* T} z^{-1}\right)}{(1 - e^{bT} z^{-1})(1 - e^{b^* T} z^{-1})} \\
&= \frac{T}{2} \cdot \frac{r + r^* + (r - r^*)\left(e^{bT} - e^{b^* T}\right) z^{-1} - (r + r^*)\, e^{(b+b^*)T} z^{-2}}{1 - \left(e^{bT} + e^{b^* T}\right) z^{-1} + e^{(b+b^*)T} z^{-2}}
\end{aligned} \tag{A.4}$$

A.1.2 Factorized Second Order Sections

FOS

$$\begin{aligned}
G_{fos}(s) &= \frac{s - \alpha_b}{s - \alpha_a} = \frac{s}{s - \alpha_a} - \frac{\alpha_b}{s - \alpha_a} \\
&\updownarrow \mathcal{L}^{-1} \\
g_{fos}(t) &= \frac{d}{dt}\left(e^{\alpha_a t} u(t)\right) - \alpha_b e^{\alpha_a t} u(t) \\
g_{fos}(t) &= e^{at}\delta(t) + \alpha_a e^{\alpha_a t} u(t) - \alpha_b e^{\alpha_a t} u(t) \\
g_{fos}(t) &= \delta(t) + (\alpha_a - \alpha_b)\, e^{\alpha_a t} u(t)
\end{aligned}$$

$$
\begin{aligned}
g_{fos}[n] &= \delta[n] + T\,(\alpha_a - \alpha_b)\, e^{\alpha_a n T} \left(u[n] - \frac{1}{2}\delta[n] \right) \\
g_{fos}[n] &= \left(1 - \frac{T}{2}\,(\alpha_a - \alpha_b) \right) \delta[n] + T\,(\alpha_a - \alpha_b)\, e^{anT} u[n] \\
&\updownarrow \mathcal{Z} \\
G_{fos}(z) &= 1 - \frac{T}{2}\,(\alpha_a - \alpha_b) + \frac{T\,(\alpha_a - \alpha_b)}{1 - e^{\alpha_a T} z^{-1}} \\
&= \frac{\left(1 - \frac{T}{2}\,(\alpha_a - \alpha_b) \right)\left(1 - e^{\alpha_a T} z^{-1} \right) + T\,(\alpha_a - \alpha_b)}{1 - e^{\alpha_a T} z^{-1}} \\
&= \frac{1 - \frac{T}{2}\,(\alpha_a - \alpha_b) - e^{\alpha_a T} z^{-1} + \frac{T}{2}\,(\alpha_a - \alpha_b)\, e^{\alpha_a T} z^{-1} + T\,(\alpha_a - \alpha_b)}{1 - e^{\alpha_a T} z^{-1}} \\
&= \frac{\frac{T}{2}\,(\alpha_a - \alpha_b) + 1 + \left[\frac{T}{2}\,(\alpha_a - \alpha_b) - 1 \right] e^{\alpha_a T} z^{-1}}{1 - e^{\alpha_a T} z^{-1}} \qquad \text{(A.5)}
\end{aligned}
$$

Second Order Section – complex-conjugate poles and zeros

$$
\begin{aligned}
G_{sos}(s) &= \frac{(s - \alpha_b)^2 + \omega_b^2}{(s - \alpha_a)^2 + \omega_a^2} \\
&= \frac{s^2}{(s - \alpha_a)^2 + \omega_a^2} - \frac{2\alpha_b\, s}{(s - \alpha_a)^2 + \omega_a^2} + \frac{\alpha_b^2 + \omega_b^2}{(s - \alpha_a)^2 + \omega_a^2} \qquad \text{(A.6)}
\end{aligned}
$$

The following transform pair and the differentiation property are expedient to perform the inverse Laplace-transform of Eq.(A.6):

$$
\frac{1}{(s - \alpha)^2 + \omega^2} \overset{\mathcal{L}}{\longleftrightarrow} \frac{1}{\omega}\, e^{\alpha t} \sin(\omega t) \qquad \text{(A.7)}
$$

$$
sF(s) \overset{\mathcal{L}}{\longleftrightarrow} f'(t) + f(0^-) \cdot \delta(t) \qquad \text{(A.8)}
$$

So the time-domain expression of Eq.(A.6) yields

$$
g_{sos}(t) = \left[f''(t) + \delta(t) f'(0^-) - 2\alpha_b \left(f'(t) + \delta(t) f(0^-) \right) + \left(\alpha_b^2 + \omega_b^2 \right) f(t) \right] u(t)\,, \qquad \text{(A.9)}
$$

where the derivatives of $f(t)$ are

$$
f(t) \;=\; e^{\alpha t} \frac{1}{\omega} \sin(\omega t) \qquad \text{(A.10)}
$$

$$
f'(t) \;=\; e^{\alpha t} \left[\frac{\alpha}{\omega} \sin(\omega t) + \cos(\omega t) \right] \qquad \text{(A.11)}
$$

$$f''(t) = e^{\alpha t}\left[\frac{\alpha^2-\omega^2}{\omega}\sin(\omega t) + 2\alpha\cos(\omega t)\right] \tag{A.12}$$

and by substitution we get:

$$\begin{aligned}
g_{sos}(t) &= \\
&= e^{\alpha_a t}\left(\tfrac{\alpha_a^2-\omega_a^2}{\omega_a}\sin(\omega_a t) + 2\alpha_a\cos(\omega_a t) - 2\alpha_b\left[\tfrac{\alpha_a}{\omega_a}\sin(\omega_a t) + \cos(\omega_a t)\right] + \tfrac{\alpha_b^2+\omega_b^2}{\omega_a}\sin(\omega_a t)\right)u(t) + \delta(t) \\
&= e^{\alpha_a t}\left(\tfrac{\alpha_a^2-\omega_a^2}{\omega_a}\sin(\omega_a t) + 2\alpha_a\cos(\omega_a t) - \tfrac{2\alpha_a\alpha_b}{\omega_a}\sin(\omega_a t) - 2\alpha_b\cos(\omega_a t) + \tfrac{\alpha_b^2+\omega_b^2}{\omega_a}\sin(\omega_a t)\right)u(t) + \delta(t) \\
&= e^{\alpha_a t}\left(\tfrac{\alpha_a^2-\omega_a^2+\alpha_b^2+\omega_b^2-2\alpha_a\alpha_b}{\omega_a}\sin(\omega_a t) + (2\alpha_a - 2\alpha_b)\cos(\omega_a t)\right)u(t) + \delta(t) \\
&= e^{\alpha_a t}\left(\underbrace{\tfrac{(\alpha_a-\alpha_b)^2-\omega_a^2+\omega_b^2}{\omega_a}}_{K_e}\cdot\sin(\omega_a t) + \underbrace{2(\alpha_a-\alpha_b)}_{K_o}\cdot\cos(\omega_a t)\right)u(t) + \delta(t) \qquad \text{(A.13)}
\end{aligned}$$

In the following the discrete-time representation of a generalized weighted sum of an exponentially-decaying sine and cosine by c.i.i.m. is derived:

$$g(t) = e^{\alpha_0 t}\left[K_e\sin(\omega_0 t) + K_o\cos(\omega_0 t)\right]u(t)$$

$$\downarrow \textit{c.i.i.m.}$$

$$\begin{aligned}
g[n] &= T e^{\alpha_0 nT}\left[K_e\sin(\omega_0 nT) + K_o\cos(\omega_0 nT)\right]\left(u[n] - \frac{1}{2}\delta[n]\right) \\
&= T\left(K_e\sin(\omega_0 nT)\,e^{\alpha_0 nT}u[n] + K_o\cos(\omega_0 nT)\,e^{\alpha_0 nT}u[n] - \frac{K_o}{2}\delta[n]\right)
\end{aligned}$$

$$\downarrow \mathcal{Z}$$

$$G(z) = T\left(K_e\frac{\sin(\omega_0 T)\,e^{\alpha_0 T}z^{-1}}{1 - 2\cos(\omega_0 T)\,e^{\alpha_0 T}z^{-1} + e^{2\alpha_0 T}z^{-2}} + K_o\frac{1 - \cos(\omega_0 T)\,e^{\alpha_0 T}z^{-1}}{1 - 2\cos(\omega_0 T)\,e^{\alpha_0 T}z^{-1} + e^{2\alpha_0 T}z^{-2}} - \frac{K_o}{2}\right)$$

$$\downarrow \text{substitution: } \tilde{z} = e^{-\alpha T}z$$

$$\begin{aligned}
G(\tilde{z}) &= T\left(K_e\frac{\sin(\omega_0 T)\tilde{z}^{-1}}{1 - 2\cos(\omega_0 T)\tilde{z}^{-1} + e^{2\alpha_0 T}z^{-2}} + K_o\frac{1 - \cos(\omega_0 T)\tilde{z}^{-1}}{1 - 2\cos(\omega_0 T)\tilde{z}^{-1} + \tilde{z}^{-2}} - \frac{K_o}{2}\right) \\
&= T\frac{K_e\sin(\omega_0 T)\tilde{z}^{-1} + K_o\cdot\left(1 - \cos(\omega_0 T)\tilde{z}^{-1}\right) - \frac{K_o}{2}\left(1 - 2\cos(\omega_0 T)\tilde{z}^{-1} + \tilde{z}^{-2}\right)}{1 - 2\cos(\omega_0 T)\tilde{z}^{-1} + \tilde{z}^{-2}} \\
&= T\frac{\frac{K_o}{2} + K_e\sin(\omega_0 T)\tilde{z}^{-1} - \frac{K_o}{2}\tilde{z}^{-2}}{1 - 2\cos(\omega_0 T)\tilde{z}^{-1} + \tilde{z}^{-2}} \qquad \text{(A.14)}
\end{aligned}$$

Applying Eq.(A.14) to Eq.(A.1.2) will lead to:

$$\begin{aligned}
G_{sos}(\tilde{z}) &= T\frac{\alpha_a - \alpha_b + \frac{(\alpha_a-\alpha_b)^2-\omega_a^2+\omega_b^2}{\omega_a}\sin(\omega_a T)\tilde{z}^{-1} - (\alpha_a - \alpha_b)\,\tilde{z}^{-2}}{1 - 2\cos(\omega_a T)\tilde{z}^{-1} + \tilde{z}^{-2}} + 1 \\
&= T\frac{(\alpha_a - \alpha_b) + \frac{(\alpha_a-\alpha_b)^2-\omega_a^2+\omega_b^2}{\omega_a}\sin(\omega_a T)\tilde{z}^{-1} - (\alpha_a - \alpha_b)\,\tilde{z}^{-2} + \frac{1}{T} - \frac{2}{T}\cos(\omega_a T)\tilde{z}^{-1} + \frac{1}{T}e^{2\alpha_a T}z^{-2}}{1 - 2\cos(\omega_a T)\tilde{z}^{-1} + e^{2\alpha_a T}z^{-2}} \\
&= T\frac{\alpha_a - \alpha_b + \frac{1}{T} + \left(\frac{(\alpha_a-\alpha_b)^2-\omega_a^2+\omega_b^2}{\omega_a}\sin(\omega_a T) - \frac{2}{T}\cos(\omega_a T)\right)\tilde{z}^{-1} - \left(\alpha_a - \alpha_b - \frac{1}{T}\right)\tilde{z}^{-2}}{1 - 2\cos(\omega_a T)\tilde{z}^{-1} + \tilde{z}^{-2}}
\end{aligned} \tag{A.15}$$

Back substitution of $\tilde{z} = e^{-\alpha_a T}z$ yields:

$$G_{sos}(z) = T\frac{\alpha_a - \alpha_b + \frac{1}{T} + \left(\frac{(\alpha_a-\alpha_b)^2-\omega_a^2+\omega_b^2}{\omega_a}\sin(\omega_a T) - \frac{2}{T}\cos(\omega_a T)\right)e^{\alpha_a T}z^{-1} - \left(\alpha_a - \alpha_b - \frac{1}{T}\right)e^{2\alpha_a T}z^{-2}}{1 - 2\cos(\omega_a T)\,e^{\alpha_a T}z^{-1} + e^{2\alpha_a T}z^{-2}} \tag{A.16}$$

SOS – conjugate-complex zeros, real poles

$$\begin{aligned}
G_{sos}(s) &= \frac{(s-\alpha)^2 + \omega}{(s-a)\,(s-b)} \\
&= \frac{s^2}{(s-a)\,(s-b)} - \frac{2\alpha_b\,s}{(s-a)\,(s-b)} + \frac{\alpha_b^2 + \omega_b^2}{(s-a)\,(s-b)}
\end{aligned} \tag{A.17}$$

$$\frac{1}{(s-a)\,(s-b)} \overset{\mathcal{L}}{\longleftrightarrow} \frac{e^{bt} - e^{at}}{a-b} \tag{A.18}$$

$$f(t) = \frac{e^{at} - e^{bt}}{a-b} \tag{A.19}$$

$$f'(t) = \frac{ae^{at} - be^{bt}}{a-b} \tag{A.20}$$

$$f''(t) = \frac{a^2e^{at} - b^2e^{bt}}{a-b} \tag{A.21}$$

$$\begin{aligned}
g_{sos}(t) &= \frac{a^2e^{at} - b^2e^{bt}}{a-b}\cdot u(t) + \delta(t) - 2\alpha\frac{ae^{at} - be^{bt}}{a-b}\cdot u(t) + \left(\alpha^2 + \omega^2\right)\frac{e^{at} - e^{bt}}{a-b}\cdot u(t) \\
&= \underbrace{\frac{(a-\alpha)^2 + \omega^2}{a-b}}_{K_a}\cdot e^{at}u(t) - \underbrace{\frac{(b-\alpha)^2 + \omega^2}{a-b}}_{K_b}\cdot e^{bt}u(t) + \delta(t)
\end{aligned}$$

$$\begin{aligned}
&\downarrow c.i.i.m.\\
g_{sos}[n] &= TK_a e^{anT}\left(u[n]-\frac{1}{2}\delta[n]\right) - TK_b e^{bnT}\left(u[n]-\frac{1}{2}\delta[n]\right) + \delta[n]\\
&= TK_a e^{anT}u[n] - TK_b e^{bnT}u[n] + \delta[n]\underbrace{\left(\frac{T}{2}\left(K_b-K_a\right)+1\right)}_{K_d}\\
&\downarrow \mathcal{Z}\\
G_{sos}(z) &= \frac{TK_a}{1-e^{aT}z^{-1}} - \frac{TK_b}{1-e^{bT}z^{-1}} + K_d\\
&= \frac{T\left(K_a-K_b\right)+K_d+\left[\left(\left(TK_b-K_d\right)e^{bT}-TK_a-K_d\right)e^{aT}\right]z^{-1}+K_d e^{(a+b)T}z^{-2}}{1-\left(e^{aT}+e^{bT}\right)z^{-1}+e^{(a+b)T}z^{-2}}
\end{aligned} \tag{A.22}$$

$$\begin{aligned}
&G_{sos}(z) =\\
&\frac{\frac{T}{2}\left(\frac{a^2-b^2}{a-b}-2\alpha\right)+1+\left[\frac{T}{2}\frac{(a-\alpha)^2+(b-\alpha)^2+2\omega^2}{a-b}\left(e^{aT}-e^{bT}\right)-e^{aT}-e^{bT}\right]z^{-1}+\left[\frac{T}{2}\left(\frac{b^2-a^2}{a-b}+2\alpha\right)+1\right]e^{(a+b)T}z^{-2}}{1-\left(e^{aT}+e^{bT}\right)z^{-1}+e^{(a+b)T}z^{-2}}\\
&b = 0 \rightarrow\\
&= \frac{\frac{T}{2}\left(a-2\alpha\right)+1+\left[\frac{T}{2}\left(a-2\alpha+2\frac{\alpha^2+\omega^2}{a}\right)\left(e^{aT}-1\right)-e^{aT}-1\right]z^{-1}+\left[\frac{T}{2}\left(2\alpha-a\right)+1\right]e^{aT}z^{-2}}{1-\left(e^{aT}+1\right)z^{-1}+e^{aT}z^{-2}}
\end{aligned} \tag{A.23}$$

REFERENCES

[AS65] M. Abramowitz and I. A. Stegun, *Handbook of Mathematical Functions: with Formulas, Graphs, and Mathematical Tables.* Dover Publications, 1965. [Online]. Available: http://www.math.sfu.ca/~cbm/aands/

[Cav96] T. Cavicchi, “Impulse invariance and multiple-order poles,” *Signal Processing, IEEE Transactions on [see also Acoustics, Speech, and Signal Processing, IEEE Transactions on]*, vol. 44, no. 9, pp. 2344–2347, September 1996.

[Chr03] K. B. Christensen, “A generalization of the biquadratic parametric equalizer,” in *Proceedings of the 115th AES Convention New York, NY, USA*, 2003.

[Dan03] J. Daniel, “Spatial sound encoding including near field effect: Introducing distance coding filters and a viable, new ambisonic format,” in *Proceedings of the 23rd International Conference of the Audio Engineering Society, Copenhagen, Denmark*, 2003.

[DH94] J. R. Driscoll and D. M. J. Healy, “Computing fourier transforms and convolutions on the 2-sphere,” *Adv. Appl. Math.*, vol. 15, no. 2, pp. 202–250, 1994.

[Eit06] E. Eitelberg, “Convolution invariance and corrected impulse invariance,” *Signal Processing*, vol. 86, no. 5, pp. 1116–1120, 2006.

[Far00] A. Farina, “Simultaneous measurement of impulse response and distortion with a swept-sine technique,” in -, 2000, pp. 18–22.

[GD05] N. A. Gumerov and R. Duraiswami, *Fast Multipole Methods for the Helmholtz Equation in Three Dimensions (Elsevier Series in Electromagnetism).* Elsevier Science, 2005.

[Har96] R. Hardin, “Mclaren’s improved snub cube and other new spherical designs in three dimensions,” *Discrete and Computational Geometry*, vol. 15, no. 4, pp. 429–441, 1996. [Online]. Available: http://www.research.att.com/~njas/doc/snub.ps

[HG06] A. Hjørungnes and D. Gesbert, “Introduction to complex-valued matrix differentiation,” 2006.

[Jac00] L. Jackson, “A correction to impulse invariance,” *Signal Processing Letters, IEEE*, vol. 7, no. 10, pp. 273–275, 2000.

[JR07] C. Jochum and P. Reiner, “Ansteuerungsfilter für den ikosaederlautsprecher,” IEM, Tech. Rep., 2007.

[KW04] P. Kassakian and D. Wessel, “Characterization of spherical loudspeaker arrays,” in *Proceedings of the 117th AES Convention San Francisco, CA, USA*, 2004.

[LD07] Z. Li and R. Duraiswami, “Flexible and optimal design of spherical microphone arrays for beamforming,” *Audio, Speech, and Language Processing, IEEE Transactions on [see also Speech and Audio Processing, IEEE Transactions on]*, vol. 15, no. 2, pp. 702–714, 2007.

[Mec00] W. Mecklenbräuker, “Remarks on and correction to the impulse invariant method for the design of iir digital filters,” *Signal Processing*, vol. 80, no. 8, pp. 1687–1690, 2000.

[MNV97] P. Muciaccia, P. Natoli, and N. Vittorio, “Fast spherical harmonic analysis: A quick algorithm for generating and/or inverting full-sky, high-resolution cosmic microwave background anisotropy maps,” *Astrophysical Journal*, vol. -, pp. –, 1997.

[Nel07] S. Nelatury, “Additional correction to the impulse invariance method for the design of iir digital filters,” *Digital Signal Processing*, vol. 17, no. 2, pp. 530–540, 2007.

[OSB99] A. V. Oppenheim, R. W. Schafer, and J. R. Buck, *Discrete-Time Signal Processing (2nd Edition).* Prentice Hall, 1999.

[PL06] S.-C. Pei and H.-S. Lin, “Minimum-phase fir filter design using real cepstrum,” *Circuits and Systems II: Express Briefs, IEEE Transactions on [see also Circuits and Systems II: Analog and Digital Signal Processing, IEEE Transactions on]*, vol. 53, no. 10, pp. 1113–1117, October 2006.

[Pol07] M. Pollow, “Variable directivity of dodecahedron loudspeakers,” Master Thesis, Institut für Technische Akustik, RWTH Aachen, 2007.

[RJ07] P. Reiner and C. Jochum, “Erfassung und evaluierung der Übersprecheigenschaften des ikosaederlautsprechers,” IEM, Tech. Rep., 2007.

[Sne94] N. Sneeuw, “Global spherical harmonic analysis by least-squares and numerical quadrature methods in historical perspective,” *Geophys. J. Int*, vol. 118, no. 3, pp. 707–716, 1994.

[WDC97] O. Warusfel, P. Dérogis, and R. Caussé, “Radiation synthesis with digitally controlled loudspeakers,” in *Proceedings of the 103rd AES Convention New York, NY, USA*, 1997.

[Wil99] E. Williams, *Fourier Acoustics: sound radiation and nearfield acoustical holography.* Elsevier, 1999.

[ZH07] F. Zotter and R. Höldrich, “Modeling radiation synthesis with spherical loudspeaker arrays,” in *Proceedings of the 19th International Congress on Acoustics Madrid, Spain*, 2007.

[ZN07] F. Zotter and M. Noisternig, “Near- and farfield beamforming using spherical loudspeaker arrays,” in *Proceedings of the 3rd Congress of the Alps Adria Acoustics Association, Graz, Austria, 2007*, 2007.

[Zot] F. Zotter, “Acoustic directivity control for spherical loudspeaker arrays,” PhD Thesis, Institute of Electronic Music and Acoustics, not puplished yet.

[ZS07] F. Zotter and A. Sontacchi, “Icosahedral loudspeaker array,” IEM, Tech. Rep. 39, 2007.

[ZSH07] F. Zotter, A. Sontacchi, and R. Höldrich, “Modeling a spherical loudspeaker system as multipole source,” in *DAGA - 33. Jahrestagung für Akustik, Stuttgart, 19.-22. März 2007*, 2007.